

AEROTHERMODYNAMICS OF TURBINE BLADE TRAILING EDGE
COOLING

A THESIS SUBMITTED TO
THE GRADUATE SCHOOL OF NATURAL AND APPLIED SCIENCES
OF
MIDDLE EAST TECHNICAL UNIVERSITY

BY

TUĞBA TUNÇEL

IN PARTIAL FULFILLMENT OF THE REQUIREMENTS
FOR
THE DEGREE OF MASTER OF SCIENCE
IN
AEROSPACE ENGINEERING

SEPTEMBER 2018

Approval of the thesis:

**AEROTHERMODYNAMICS OF TURBINE BLADE TRAILING EDGE
COOLING**

submitted by **TUĞBA TUNÇEL** in partial fulfillment of the requirements for the degree of **Master of Science in Aerospace Engineering Department, Middle East Technical University** by,

Prof. Dr. Halil Kalıpçılar
Dean, Graduate School of **Natural and Applied Sciences**

Prof. Dr. Ozan Tekinalp
Head of Department, **Aerospace Engineering**

Asst. Prof. Dr. Harika Senem Kahveci
Supervisor, **Aerospace Engineering Department, METU**

Examining Committee Members:

Prof. Dr. Mehmet Cevdet Çelenligil
Aerospace Engineering, METU

Asst. Prof. Dr. Harika Senem Kahveci
Aerospace Engineering, METU

Assoc. Prof. Dr. Oğuz Uzol
Aerospace Engineering, METU

Assoc. Prof. Dr. Metin Yavuz
Mechanical Engineering, METU

Asst. Prof. Dr. Sıtkı Uslu
Mechanical Engineering, TOBB ETU

Date:

I hereby declare that all information in this document has been obtained and presented in accordance with academic rules and ethical conduct. I also declare that, as required by these rules and conduct, I have fully cited and referenced all material and results that are not original to this work.

Name, Last Name: TUĞBA TUNÇEL

Signature :

ABSTRACT

AEROTHERMODYNAMICS OF TURBINE BLADE TRAILING EDGE COOLING

TUNÇEL, TUĞBA

M.S., Department of Aerospace Engineering

Supervisor : Asst. Prof. Dr. Harika Senem Kahveci

SEPTEMBER 2018, 81 pages

It is known that the thermal efficiency of gas turbines strongly depends on the turbine entry temperature of the working fluid. This has resulted in increased turbine working temperatures, and peak temperatures in advanced gas turbines have been well above maximum allowable metal temperatures for quite some time. For turbine blades to survive while operating beyond these material temperature limits, internal and external cooling techniques have been developed. Due to structural and aerodynamic restrictions, improving trailing-edge cooling methods creates a challenge for the designers. In modern turbine blades, pressure side cutbacks with film cooling slots stiffened with lands and pin fins embedded in passages are used to cool trailing edges. In literature, thermal improvements obtained by slots, lands and similar internal structures have been investigated in detail since the main purpose has been to promote cooling. But, when the performance of a gas turbine is considered, aerodynamic enhancements are as important as thermal performance. Regarding that, this thesis focuses on both aerodynamic and thermal aspects of a turbine blade trailing-edge section cooling. The internal structure studied consists of staggered arrays of

pins, and lands and airfoil-shaped blockages in front of the trailing edge slots right at the exit. The pins used are of cylindrical, elliptical, and airfoil shape, and have different sizes. A study using Computational Fluid Dynamics (CFD) was performed to investigate the flow structure and heat transfer both inside the passage and outside in the vicinity of trailing-edge slots. With the goal of choosing an optimal pin fin configuration that is aerothermodynamically more advantageous for slot film cooling, this thesis provides a thorough investigation that would be of interest to the turbine designers.

Keywords: Turbine Blade Cooling, Trailing Edge, Pin Fin Cooling, Film Cooling, Computational Fluid Dynamics

ÖZ

TÜRBİN KANADI FIRAR KENARI SOĞUTMASININ AEROTERMODİNAMİĞİ

TUNÇEL, TUĞBA

Yüksek Lisans, Havacılık ve Uzay Mühendisliği Bölümü

Tez Yöneticisi : Dr. Öğr. Üyesi Harika Senem Kahveci

Eylül 2018 , 81 sayfa

Gaz türbinlerinin termal verimliliğinin, çalışma akışkanının türbin giriş sıcaklığına bağlı olduğu bilinmektedir. Bu durum türbin çalışma sıcaklıklarında artışa ve gelişmiş gaz türbinlerindeki zirve sıcaklıklarının metallerin dayanabileceği maksimum sıcaklıkları aşmasına neden olmuştur. Türbin kanatlarının malzeme sıcaklık sınırlarının ötesinde çalışabilmesi için iç ve dış soğutma teknikleri geliştirilmiştir. Yapısal ve aerodinamik kısıtlamalar yüzünden firar kenarı soğutma yöntemlerinin geliştirilmesi tasarımcılar için zorlu bir görev oluşturmaktadır. Modern türbin kanatlarının firar kenarlarının soğutulmasında, film soğutması oluklarının bulunduğu kesilmiş basınç kenarları ve pin fin yapıları kullanılmaktadır. Literatürdeki çalışmalarda oluk, ada ve benzer kanat içi yapılar sayesinde elde edilebilecek potansiyel termal iyileştirmeler, soğutmanın daha iyi yapılabilmesi amacıyla şu ana kadar detaylı bir şekilde incelenmiştir. Ancak, gaz türbinlerinin tüm performansı düşünüldüğünde, bu bölgedeki aerodinamik iyileştirmeler termal iyileştirmeler kadar önem teşkil etmektedir. Bu durumu göz önünde bulundurarak bu tez, firar kenarı soğutma yapısını aerothermal açıdan incelemektedir. Çalışılan iç yapı saptırılmış pin dizinleri, adalar ve olukların

önünde bulunan kanat şeklindeki tıkaçlardan oluşmaktadır. Kullanılan pinler dairesel, eliptik ve kanat şeklindedir. Eliptik ve kanat şeklindeki pinlerin farklı boyutlardaki versiyonları da bulunmaktadır. Pinlerin akış yapıları ve ısı transferi performanslarını incelemek için kanal içinde ve firar kenarı yakınlarında Hesaplamalı Akışkanlar Dinamiği (HAD) kullanan bir çalışma yapılmıştır. Bu tez oluklu film soğutması için aerotermodinamik açıdan optimum pin şeklini seçmek amacıyla olan tasarımcılar için detaylı bir çalışma sunmaktadır.

Anahtar Kelimeler: Türbin Kanat Soğutması, Firar Kenarı, Pin Fin Soğutma, Film Soğutma, Hesaplamalı Akışkanlar Dinamiği

To My Beloved Ones

ACKNOWLEDGMENTS

First and foremost, I would like to express my most deepest gratitude and thanks to my supervisor Asst. Prof. Dr. Harika S. Kahveci for her guidance, support and limitless help she provided me during my academic researches. I will always consider myself very lucky to be her first graduate student.

I would also like to thank my committee members Prof. Dr. Mehmet Cevdet Çelenligil, Assoc. Prof. Dr. Oğuz Uzol, Assoc. Prof. Dr. Metin Yavuz and Asst. Prof. Dr. Sıtkı Uslu for their valuable suggestions and insights about this work.

I am so grateful to my friends Metehan Yayla, Ezgi Orbay Akcengiz, Ayşe Usta Yayla, Alper Açııcı, Berk Gür, Zeynep Ünal, Ayşe Hazal Altuğ Yalçın, Özgür Yalçın, Özcan Yırtıcı, Ahmet Arda Akay, Tansu Sevine, Derya Kaya, Engin Leblebici, Ali Büyükköçak ,and Levent Şahin for helping me survive all the stress and not letting me give up.

My special thanks to Çağla Ceren Ceyhan, and Melek Dicle Özcan for their invaluable support, and the moments shared. My special thanks are extended to my oldest friend Elif Yağmur Tatkan for always being there for me and to Selva Sargın Güçlü for her cheering and companion. Also I would like to thank my special friend Mehmetcan Demir for his endless love, support and patience.

Finally, I would like to express my deepest gratitude to my mother, my father and my brother for their never ending support. Without them, I would not have achieved this thesis like many of other things that I have in my life.

TABLE OF CONTENTS

ABSTRACT	v
ÖZ	vii
ACKNOWLEDGMENTS	x
TABLE OF CONTENTS	xi
LIST OF TABLES	xiv
LIST OF FIGURES	xv
LIST OF ABBREVIATIONS	xix
CHAPTERS	
1 INTRODUCTION	1
1.1 Motivation	1
1.2 Objective	4
1.3 Thesis Outline	5
2 LITERATURE SURVEY	7
2.1 Internal Cooling	7
2.2 External Cooling	10
3 METHODOLOGY	15
3.1 Mathematical Modeling	15
3.2 Numerical Modeling	16

3.3	Validation Case	19
3.3.1	Internal Cooling	21
3.3.1.1	Boundary Conditions	21
3.3.1.2	Geometry and Meshing	22
3.3.1.3	Solution Convergence	25
3.3.2	External Cooling	26
3.3.2.1	Boundary Conditions	26
3.3.2.2	Geometry and Meshing	26
3.3.2.3	Solution Convergence	29
3.4	Comparison Cases	30
3.4.1	Internal Cooling	30
3.4.1.1	Boundary Conditions	30
3.4.1.2	Geometry and Meshing	31
3.4.1.3	Solution Convergence	35
3.4.2	External Cooling	35
3.4.2.1	Boundary Conditions	35
3.4.2.2	Geometry and Meshing	37
3.4.2.3	Solution Convergence	38
4	INTERNAL COOLING ANALYSIS & RESULTS	41
4.1	Validation	41
4.2	Aerodynamic Results From Comparison Cases	43
4.3	Thermal Results From Comparison Cases	50
5	EXTERNAL COOLING ANALYSIS & RESULTS	55

5.1	Validation	55
5.2	Aerodynamic Results From Comparison Cases	56
5.3	Thermal Results From Comparison Cases	65
6	CONCLUSIONS	73
	REFERENCES	77

LIST OF TABLES

TABLES

Table 3.1	Experimental Conditions From Ref [1]	22
Table 3.2	External Flow Experimental Conditions From Ref [1]	26
Table 3.3	Internal Flow Comparison Case Boundary Conditions	31
Table 3.4	Internal Comparison Case Model Dimensions	32
Table 3.5	Mass Flow Averaged Slot Static Temperatures For Different Pin Shapes	36

LIST OF FIGURES

FIGURES

Figure 1.1	Variation Of TET And Cooling Methods Over The Years [2]	2
Figure 1.2	Cooling Methods On A Turbine Blade [2]	3
Figure 3.1	Schematic Of Experimental Model [3]	20
Figure 3.2	Schematic Of Validation Model a) Top View , b) Isometric View	21
Figure 3.3	Computational Domain Used For Internal Validation Case	23
Figure 3.4	Meshing Used For Internal Validation Case	24
Figure 3.5	Streamwise Velocity Profiles For Internal Validation Case Grid Sensitivity Study	24
Figure 3.6	RMS Residuals For Internal Validation Case	25
Figure 3.7	Computational Domain Used For External Validation Case	27
Figure 3.8	Grid Used In External Validation Case	28
Figure 3.9	Streamwise Velocity Profiles For External Validation Case Grid Sensitivity Study	29
Figure 3.10	RMS Residuals For External Validation Case	29
Figure 3.11	Computational Models Used In Internal Comparative Study a) Cir- cular, b) Elliptical, c) Airfoil Shaped, d) Small-Elliptical, e) Small-Airfoil Shaped	33

Figure 3.12 Streamwise Velocity Profiles For Internal Comparison Case Grid Sensitivity Study	34
Figure 3.13 Near-pin Location Zoomed-in Views Of Grids Used In Comparative Study a) Circular, b) Elliptical, c) Airfoil Shaped, d) Small-Elliptical, e) Small-Airfoil Shaped	34
Figure 3.14 RMS Residuals For Internal Comparison Case	35
Figure 3.15 Blowing Area Velocity Profiles a) Circular, b) Elliptical, c) Airfoil Shaped, d) Small-Elliptical, e) Small-Airfoil Shaped	36
Figure 3.16 Streamwise Velocity Profiles For External Comparison Case Grid Sensitivity Study	37
Figure 3.17 Grid Used In External Comparison Case	38
Figure 3.18 RMS Residuals For External Comparison Case	39
Figure 4.1 Non-Dimensional Streamwise Velocity Contours a) Experimental (Fig. 3 of [3]) , b) Predictions	42
Figure 4.2 Streamwise Velocity Contours a) Circular, b) Elliptical, c) Airfoil Shaped, d) Small-Elliptical, e) Small-Airfoil Shaped	43
Figure 4.3 Non-Dimensionalized Streamwise Vorticity Contours a) Circular, b) Elliptical, c) Airfoil Shaped, d) Small-Elliptical, e) Small-Airfoil Shaped	45
Figure 4.4 Mass Flow-Averaged ψ In Streamwise Direction	46
Figure 4.5 Entropy Contours a) Circular, b) Elliptical, c) Airfoil Shaped, d) Small-Elliptical, e) Small-Airfoil Shaped	47
Figure 4.6 Loss Split Per Region	48
Figure 4.7 Mass Flow-Averaged Entropy In Streamwise Direction	50

Figure 4.8 Heat Transfer Coefficient Contours a) Circular, b) Elliptical, c) Airfoil Shaped, d) Small-Elliptical, e) Small-Airfoil Shaped	51
Figure 4.9 Normalized Nusselt Numbers For Pin Arrays a) Experiment (Fig. 4 of [4]), b) Predictions	52
Figure 4.10 Loss And Thermal Comparison Of Pin Arrays	53
Figure 5.1 Non-Dimensional Streamwise Velocity Contours Downstream Of Slot Exit a) Experimental (Fig. 3 of [3]) , b) Predictions	56
Figure 5.2 Streamwise Velocity Contours Downstream Of Slot Exit a) Circular, b) Elliptical, c) Airfoil Shaped, d) Small-Elliptical, e) Small-Airfoil Shaped	57
Figure 5.3 Streamwise Non-Dimensional Vorticity Contours With Velocity Vectors At Slot Exit a) Circular, b) Elliptical, c) Airfoil Shaped, d) Small-Elliptical, e) Small-Airfoil Shaped	58
Figure 5.4 Streamwise Non-Dimensional Vorticity Contours With Velocity Vectors At 1H Downstream Of Slot Exit a) Circular, b) Elliptical, c) Airfoil Shaped, d) Small-Elliptical, e) Small-Airfoil Shaped	59
Figure 5.5 Streamwise Non-Dimensional Vorticity Contours With Velocity Vectors At 2H Downstream Of Slot Exit a) Circular, b) Elliptical, c) Airfoil Shaped, d) Small-Elliptical, e) Small-Airfoil Shaped	60
Figure 5.6 Streamwise Non-Dimensional Vorticity Contours With Velocity Vectors At 3H Downstream Of Slot Exit a) Circular, b) Elliptical, c) Airfoil Shaped, d) Small-Elliptical, e) Small-Airfoil Shaped	61
Figure 5.7 Streamwise Non-Dimensional Vorticity Contours With Velocity Vectors At 4H Downstream Of Slot Exit a) Circular, b) Elliptical, c) Airfoil Shaped, d) Small-Elliptical, e) Small-Airfoil Shaped	62

Figure 5.8 Streamwise Non-Dimensional Vorticity Contours Downstream Of Slot Exit a) Circular, b) Elliptical, c) Airfoil Shaped, d) Small-Elliptical, e) Small-Airfoil Shaped	64
Figure 5.9 Total Temperature Contours Downstream Of Slot Exit a) Circular, b) Elliptical, c) Airfoil Shaped, d) Small-Elliptical, e) Small-Airfoil Shaped	65
Figure 5.10 Total Temperature Contours With Different Temperature Ranges for Case (a)	66
Figure 5.11 Film Cooling Effectiveness Contours At Breakout Surface a) Circular, b) Elliptical, c) Airfoil Shaped, d) Small-Elliptical, e) Small-Airfoil Shaped	67
Figure 5.12 Film Cooling Effectiveness Contours at Land Side Wall a) Circular, b) Elliptical, c) Airfoil Shaped, d) Small-Elliptical, e) Small-Airfoil Shaped	68
Figure 5.13 Laterally-Averaged Film Cooling Effectiveness at Breakout Surface	69
Figure 5.14 X/H Locations	69
Figure 5.15 Laterally-Averaged Film Cooling Effectiveness on Land Side Wall .	70
Figure 5.16 Loss And Thermal Comparison Of External Cooling Performance of Pin Arrays	71

LIST OF ABBREVIATIONS

c	Log Layer Constant
D	Pin Diameter (mm)
F_2	Blending Function
h_{tot}	Total Enthalpy (m^2/s^2)
H	Channel Height (mm)
H_p	Pin Height (mm)
HTC	Heat Transfer Coefficient
k	Turbulent Kinetic Energy
k_f	Thermal Conductivity of Fluid (W/mK)
L	Total Streamwise Length of Internal Cooling Domain (mm)
Nu	Nusselt Number
P_T	Inlet Total Pressure (Pa)
$P_{T,l}$	Local Total Pressure (Pa)
q''	Wall Heat Flux (W/m^2)
s_e	Mass Flow-Averaged Coolant Exit Entropy (J/kgK)
s_i	Mass Flow-Averaged Coolant Inlet Entropy (J/kgK)
s_l	Mass Flow-Averaged Local Entropy (J/kgK)
s_{up}	Mass Flow-Averaged Upstream Local Entropy (J/kgK)
S	Magnitude of Strain Rate
S_{ij}	Strain Rate Tensor
S_p	Streamwise Distance Between Pins (mm)
T_{bulk}	Bulk Temperature (K)
T_c	Coolant Static Temperature at Slot Exit (K)
$T_{s\infty}$	Main Flow Static Temperature (K)

T_{wall}	Wall Temperature (K)
u_{bulk}	Bulk Velocity (m/s)
u_i	Coolant Inlet Velocity (m/s)
u_s	Streamwise Coolant Velocity (m/s)
u_s'	Non-Dimensional Streamwise Velocity
u_τ	Friction Velocity (m/s)
U	Velocity (m/s)
x	Axial Coordinate (mm)
X	Axial Distance from Slot Exit (mm)
X_p	Lateral Distance Between Pins (mm)
y	Distance to Nearest Wall (m)
β	Flux Limiter Parameter
$\Delta \vec{r}$	Vector Between Integration Point and Upwind Node
η	Film-Cooling Effectiveness
κ	Von Karman Constant
ν	Kinematic Viscosity (m^2/s)
ν_t	Eddy Viscosity (m^2/s)
ρ	Density (kg/m^3)
τ	Shear Stress (N/m^2)
φ	Scalar Variable
Ψ	Total Pressure Coefficient
ω	Specific Dissipation Rate
ω_s	Streamwise Vorticity ($1/s$)
ω_s'	Non-Dimensional Streamwise Vorticity

CHAPTER 1

INTRODUCTION

In this chapter, the importance of turbine cooling and conventional cooling techniques used in modern turbine blades is summarized. Then, the challenges specific to the trailing-edge cooling, which is the motivation behind this thesis, are explained. Regarding the constraints of the trailing-edge cooling, the objectives of this work are mentioned. Finally, the organization of the thesis is presented.

1.1 Motivation

Gas turbine engines started to be used for power generation in early 1940's. Since then the need for improving performance of gas turbines has continued day by day. This need drives the gas turbine industry and leads to new technological challenges. One of them is the constant increase of turbine entry temperature (TET) levels. Designers prefer to increase TET because this method does not only increase the power output but also decreases the fuel consumption. The challenge about TET is related to material limitations. Peak temperatures in advanced gas turbines have been around 2000 K or even more for quite some time, and these levels are well above the maximum allowable metal temperatures.

To withstand excessive temperatures, different cooling techniques have been developed and used in modern turbine blades. The increase of TET and the evolution of cooling techniques over the years is summarized in Figure 1.1. Development of cooling methods started with smooth cooling holes but this was not enough as temperatures continued to rise. With new approaches like turbulated cooling-hole designs, the aim of cooling blades was achieved, but this time thermal stresses on the blades

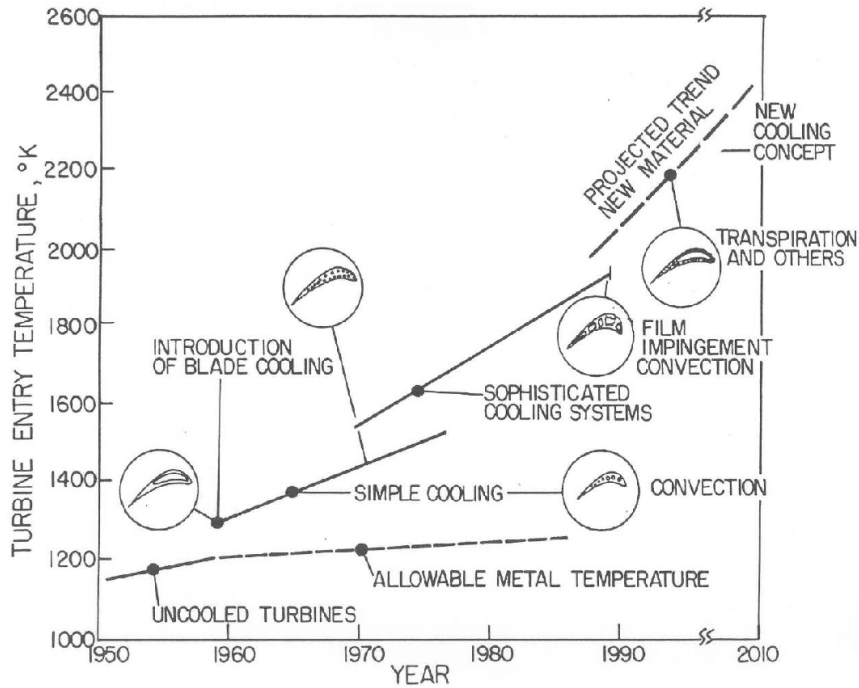


Figure 1.1: Variation Of TET And Cooling Methods Over The Years [2]

became an issue. This new problem has created new constraints for the designers. As methods advanced additional complexities were introduced into cooling technologies, leading to today's highly sophisticated turbine cooling systems.

Modern turbine blades are equipped with a combination of various cooling techniques to prevent any potential means of failure. In general, these techniques are divided into two categories as internal cooling and external cooling. Internal cooling is achieved by circulating coolant through cooling holes that are called serpentine passages. Coolant inside of the blade is blown through small holes on the blade called film-cooling holes in order to externally cool the blade.

The main aim of internal cooling is to prevent overheating of the blade by creating a convective heat transfer between coolant and the blade. Mostly used internal cooling methods are impingement cooling, rib-turbulated cooling, and pin-fin cooling. In impingement cooling, a high velocity coolant is impinged through the rows of small holes into the interior surface of the blade. This method is only used in the leading edge part of the blades due to structural constraints and high centrifugal loads. To increase heat transfer, various shaped ribs are placed on inner walls of serpentine

passages, which is referred to as rib-turbulated cooling. These ribs enhance heat transfer by both increasing the surface area and the turbulence level of the coolant. Rib-turbulated cooling is generally implemented on the mid-section of the blades. The idea behind the pin-fin cooling and the rib-turbulated cooling is the same, but due to the limited space and the structural constraints of the trailing edge region, pin fins are used instead of rib turbulators. The internal cooling configurations are shown in Figure 1.2.

Unlike the internal cooling, the main purpose of the external cooling is to protect outside of the blade from direct contact with hot gasses. It is achieved by injecting coolant air used for internal cooling onto the surface of the blade through film cooling holes located on the blade. Injected coolant creates a protective layer on the surface. By this way, the heat load on the surface is decreased and since the blade is cooled from both inside and outside, the thermal stresses generated inside of the blade are reduced. Figure 1.2 shows the most conventional film cooling hole locations.

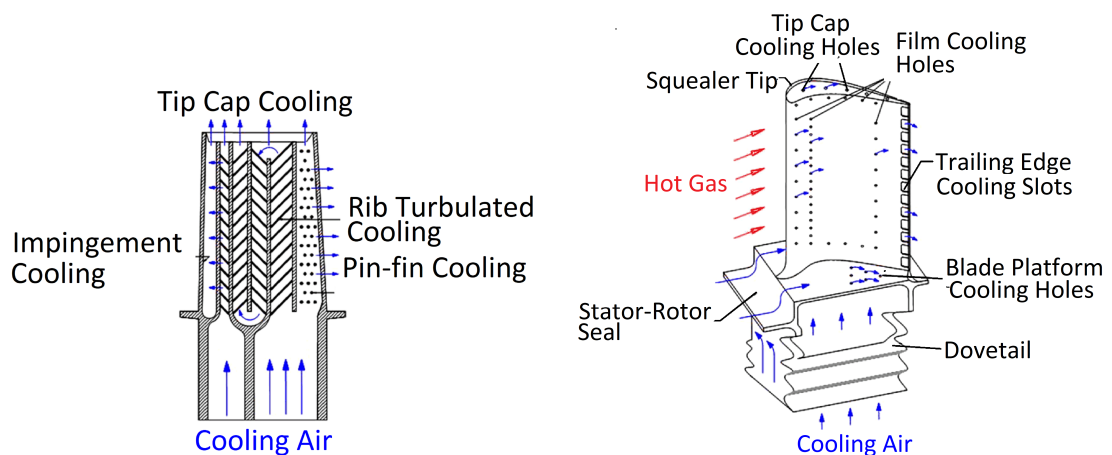


Figure 1.2: Cooling Methods On A Turbine Blade [2]

Cooling each region of a blade has its own challenges, but among them the trailing-edge region is the most difficult to cool down. The difficulty is due to the contradictory requirements of aerodynamic, thermal, and structural aspects. To withstand high centrifugal loads, the trailing edge region has to be structurally rigid. But, from an aerodynamic perspective, it should be as thin as possible to reduce mixing losses downstream of the blade. Regarding the thermal issues, the thin trailing edge causes high convective fluxes due to low heat capacity, which leads to burns on the blade and

eventually the failure. Because of those conflicts, the design of trailing-edge cooling systems requires a tradeoff between the aerodynamic losses and thermal enhancements.

The most common and effective trailing-edge cooling method is slot film cooling. The pressure side of the blade is partially cut out along the blade chord, and various shaped-ribs called lands are placed periodically along the span. Coolant is injected out of the cutback surface through the openings between the lands, which are called slots. The sprayed coolant creates a buffer layer between the hot mainstream and the blade surface [5]. To enhance heat transfer and to counteract the structural weakening caused by thinning the trailing edge, pin fins are used in the internal cooling passages at this region.

1.2 Objective

Performance of pin-fin cooling and slot film cooling depends on many variables. For pin-fin cooling, most important parameters are the pin shape, pin array orientation, pin spacing, and the channel aspect ratios. Related to slot film cooling, critical factors are the blowing ratio, lip thickness-to-slot height ratio, land shape, lip shape, and the lip thickness variation. Those parameters both affect the thermal and aerodynamic performance of the blade. As stated in the motivation part, trailing-edge cooling is a trade-off between heat transfer and aerodynamic losses generated by the cooling system.

In this thesis, aerodynamic and thermal performances of circular, elliptic and NACA 0033 profile shaped pins are studied. The circular pins have been the most-widely used pin shape in internal cooling, followed by elliptical shapes with a more limited usage. The airfoil shape is rather more novel shape type that has been studied scarcely. The blockages in the studied model have the specific airfoil profile NACA 0033 and this profile is mimicked in the whole pin array. The study is divided into two parts investigating the effects of 1) internal cooling, and 2) external cooling. First part of the study considers the effects of those three shapes inside of the internal cooling passages. The major aim in this part is to find the best pin shape and size combina-

tion regarding the pressure losses versus heat transfer enhancement. In order to do this, the aerodynamic loss characteristics of pins and the distribution of heat transfer coefficients in the passage are investigated. The second part considers the external trailing-edge cooling. The major aim here is to understand the effect of different inlet coolant profiles on the slot film-cooling performance. The inlet profiles are generated by five different pin arrays, and the resulting external flow features downstream of the slots are studied from the aerodynamic and thermal perspectives. In this way, the external cooling performance of various internal pin-fin configurations is investigated.

1.3 Thesis Outline

This thesis consists of six chapters. Chapter 1 introduces the need for turbine blade cooling and gives brief information about conventional cooling technologies specifically used for the blade trailing-edge section. Then, the objectives of this work are summarized.

Chapter 2 presents the overview of literature that has studied the internal and external trailing-edge cooling. The internal cooling section particularly focuses on the size, shape, and the orientation effects of pin-fin cooling. In the external cooling section, research concerning the slot film cooling is reviewed.

In Chapter 3, the mathematical and numerical modeling approaches applied in this thesis are explained. The experimental case used as the validation case is explained, and the solid model and the boundary conditions used for the numerical modeling are presented.

Chapters 4 and 5 are devoted to the findings derived from the CFD analysis. The presentation of results is divided into two parts. In the first part, the aerodynamic findings are discussed followed by the second part where the thermal findings are demonstrated.

Chapter 6 summarizes the conclusions drawn from this study and gives suggestions for future work.

CHAPTER 2

LITERATURE SURVEY

In this chapter, the type of studies that have been done so far related to trailing-edge cooling methods are summarized. The studies are divided into two parts as internal and external cooling. In the internal cooling, the research specific to pin-fin cooling is reviewed. The external cooling part focuses on the studies that investigate slot film cooling.

2.1 Internal Cooling

Coolant channel structures, especially circular pin fins, were studied in great detail in literature since they are being used in many other cooling applications as well. An early study done by Brigham and VanFossen [6] focused on the pin length-to-diameter ratio and found that this ratio has a major effect on heat transfer coefficient. Further, they showed that when this ratio is below 2, Nusselt number depends on the Reynolds number, but not on the length-to-diameter ratio anymore. Metzger et al. [4] performed experiments to investigate the heat transfer performance of arbitrary combinations of circular pins by changing the diameter and the stream-wise spacing of pins in constant and converging flow areas, separately. Then, they used a superimposition technique to obtain the Nusselt number for complex combinations of circular pin-fin arrays. Armstrong and Winstanley [7] performed a review on the turbine cooling applications using a staggered-array of pin fins. Their findings showed that the research results on pin-fin heat transfer and flow friction were not enough to develop generalized heat transfer and friction-loss correlations. An experimental investigation for heat transfer capabilities of partial-length circular pin fins was performed by Arora

and Abdel Messeh [8]. As a result of these experiments, it was found that both heat transfer and pressure loss are inversely proportional to the pin-tip clearance. Ligrani and Mahmood [9] focused on the effects of the coolant-to-wall temperature ratio on the Nusselt number and friction factor. They concluded that as this ratio decreased, the Nusselt number increased while the friction factor decreased. Chyu [10] compared circular pins with and without endwall fillet radius, and he discovered that the pins without the endwall fillet caused higher heat transfer and lower pressure loss.

Although circular pins are the most-frequently used turbulence promoters due to their easy manufacturing, in order to further increase heat transfer, the effects of different pin shapes have been investigated by different researchers. A major study on effects of pin shape on pressure loss and heat transfer was conducted by Metzger et al. [11]. In this work, experiments were performed for two families of array geometries. Pressure loss and heat transfer coefficients of oblong-shaped pins and circular pins were compared. It was found that although heat transfer performance of oblong-shaped pins are 20% higher than that of circular pins, the resulting pressure loss is 100 % higher, which is a noticeable disadvantage to the use of such pins at regions where a trade-off exists between heat transfer and aerodynamics. In addition, they studied the arrangement of circular pin fins, and found that changing it from an inline to a staggered configuration not only increased the heat transfer, but also decreased the pressure loss at the same time.

Chyu et al. [12] conducted experiments with cubic and diamond-shaped pins. Since they result in a high heat transfer enhancement while maintaining a moderate pressure penalty, cubic pins can be used as an alternative to circular pins. A similar comparison between elliptic and circular pins was done by Li et al. [13]. Elliptical pins had a major-to-minor axis ratio of 1.78 and the same circumference with that of the circular pins. Heat transfer and resistance coefficients of both pin shapes were calculated using experimental measurements. It was found that for the investigated range of Reynolds numbers between 1000 to 10000, elliptical pins display both higher convective heat transfer performance and less flow resistance.

In another study, Uzol and Camci [14] used elliptical pins having the same frontal area with that of circular pins, rather than the circumference. They investigated the

reasons for the improved aerodynamic performance of elliptical pins. Studying the flow structures around pins, they concluded that the wakes of circular pins are higher than those of elliptical pins, which enhance heat transfer but create higher pressure loss.

Chen et al. [15] proposed drop-shaped pins as an alternative to circular pins. In their research, naphthalene sublimation technique was used to investigate the flow field. The results showed that depending on their relative spacing, drop-shaped pins demonstrate 41 % to 52 % less flow resistance with increased overall heat transfer performance in the studied Reynolds number range.

More recently, Ling et al. [3] measured the three-dimensional velocity and concentration fields of the flow through the pressure-side cutback region of a NACA-0012 airfoil, with a plenum located inside of the airfoil consisting of an array of four rows of staggered pin fins. The study focused on the flow characteristics at the slot exit and on the breakout surface. Comparisons between two trailing edge configurations, one with thin straight lands and airfoil-shaped blockages and one without, revealed that the thinner lands of the former airfoil resulted in higher spanwise average surface effectiveness, but in lower coolant concentration uniformity. In a subsequent study, Ling et al. [16] performed RANS modeling of the same trailing edge slot configuration with and without blockages. They showed that the $k-\omega$ SST turbulence model under-predicts the turbulent viscosity both throughout the pin-fin array and on the breakout surface resulting in inaccurate velocity calculations and coolant concentration. Likewise, Ames and Dvorak [17] performed experiments searching for the reasons behind heat transfer enhancement of pin fins. They modeled their experiments using conventional turbulence models. Their findings suggest that all of the turbulence models they used under-predict both heat transfer and pressure drop.

As in [16] [17], there have been other attempts to approach the problem from a numerical standpoint in addition to experimentation. In their study, Martini et al. [18] modeled three different internal cooling structures using unsteady detached eddy simulation (DES). Their results showed that for examining discharge coefficients, steady RANS models could be used as an alternative to time-consuming unsteady DES calculations. Wang et al. [19] performed both experiments and computations with five

different pin geometries with the same cross-sectional areas. While flow structures showed distinct differences between the data and the predictions, the pressure loss behaviors were found to be in good agreement. Their findings suggest that drop-shaped pins can be used as an alternative to circular pins. More recently, Fernandes et al. [20] studied the accuracy of the well-known turbulence models in the prediction of heat transfer rates and pressure distribution on the surface of pin fins. They concluded that the quadratic realizable $k-\epsilon$ and the $k-\omega$ SST turbulence models estimate the heat transfer rates the most accurately.

Pin shapes other than circular ones did not get enough attention because manufacturing of different shapes in micro scales was a problem. But with a new manufacturing technique called "Direct Metal Laser Sintering " (DMLS), it is now possible to produce complex shapes in micro scales. This new technique, opened a new research area in pin fin cooling. Nowadays, researchers in this area are trying to find alternative shapes that have better aerothermodynamic performance. In their recent work Ferster et al. [21] conducted experiments for triangular, star shaped and dimpled spherical-shaped pin fins manufactured with DMLS technique. They investigated the effects of pin geometry, spacing, and number of pins on heat transfer and pressure loss performance. Their experiments showed that triangular pins outperformed star shaped and dimpled spherical pins in heat transfer augmentation. Besides experimental results were compared with cylindrical pin results from an old study [22], which proved that their heat transfer and pressure loss performances were similar which makes triangular pins desirable since weight of triangular pins would be less than circular ones having the same wetted area.

2.2 External Cooling

Trailing edge external cooling configurations are investigated in great detail due to their direct impact on turbine stage efficiency. A notable study related to trailing-edge cooling was done by Cunha and Chyu [23]. They developed analytical solutions for the temperature distribution of four simple trailing-edge cooling configurations that are solid wedge shape without discharge, wedge with slot discharge, wedge with discrete hole discharge, and wedge with pressure-side cutback slot discharge. They have

also done experiments to understand the details of a more complicated trailing-edge cooling configuration, which includes an internal cooling channel with pins and an external cooling structure with pressure-side cutback supported with lands. They claim that with a good selection of the design parameters, cutbacks with lands configuration is a desirable trailing-edge cooling method regarding structural and aerodynamic performances.

A leading study in slot film-cooling area was done by Kacker and Whitelaw [24]. In their study, they conducted experiments to find a correlation between adiabatic wall effectiveness and slot lip thickness-to-slot height ratio. They concluded that those two parameters are inversely proportional to each other. In a similar study, Sivasegaram and Whitelaw [25] considered the effects of slot lip thickness-to-slot height ratio and the injection angle on film cooling effectiveness. Their findings on slot lip thickness-to-slot height ratio agree with the earlier study. Besides, they showed that film-cooling effectiveness of an angled slot can be greater than a tangential slot.

More recently, Horbach et al. [26] investigated the aerodynamic and heat transfer performance of different lip geometries. They conducted experiments by considering four lip thicknesses and three lip shapes. This study revealed that the lip thickness affects the mixing of coolant and the main flow at the slot. As the lip thickness increases, the wake region grows, which increases pressure loss and decreases film-cooling performance. They also found that the lip shape does not considerably affect the thermal and aerodynamic performance of film cooling. In their following study, Horbach et al. [27] used the same setup with three different pin fin configurations which are circular and streamwise and spanwise-oriented elliptical pins to see the effect of internal pin fin configuration on the external film-cooling performance. By taking circular pins as a reference point, the streamwise-oriented pins have higher discharge coefficients and lower heat transfer performance, while the spanwise-oriented pins have lower discharge coefficients and higher heat transfer performance. Regarding film-cooling effectiveness, the streamwise-oriented and circular pins perform similarly whereas the spanwise configuration displays poor performance.

A very detailed analysis of slot film cooling was performed by Taslim et al. [28]. Their study concerns about the effects of the injection angle, slot lip thickness-to-

height ratio, slot width-to-height ratio, blowing ratio, and the coolant-to-mainstream density ratio on film effectiveness. They applied constraints on parameters considering the general engine operation conditions and conducted a series of experiments parametrically. The experiments revealed that film effectiveness is insensitive to the density ratio and slot aspect ratios, while lip thickness-to-height ratio and the injection angle have considerable impact on film effectiveness. Based on their results, they developed a correlation between lip thickness-to-height ratio and film effectiveness, and they showed that the correlation changes depending on the blowing ratio. They also found that 8.5 is the optimum injection angle for the best film effectiveness.

A similar research was done by Fiala et al. [29], which investigated how the blowing rate, Reynolds number and the external turbulence affect heat transfer and film-cooling effectiveness. They focused on the top and side surfaces of letterbox-shaped lands. According to their results, film effectiveness can be correlated with blowing ratio. It is directly proportional at land tops while inversely proportional at land sides. Moreover, they found that the external turbulence does not have a considerable influence on the land film-effectiveness levels.

Yang and Hu [30] conducted experiments by using Pressure Sensitive Paint Technique to explore influence of existence of lands on film-cooling performance. Experiments were performed with and without land configurations for blowing ratios between 0.4 and 1.6. Their results claim that as the blowing ratio increases, the streamwise film effectiveness increases but the spanwise effectiveness decreases. The existence of the lands empowers film-cooling performance in the streamwise direction since the lands enforce coolant to spread in the slot channel. But, at the same time, the lands restrain the expansion of coolant in the spanwise direction, which worsens film-cooling effectiveness. Although their findings support that overall heat transfer performance of design without land case is better, they still recommend using lands to ensure structural strength of blades.

Although most of the research related to the trailing-edge cooling focus on heat transfer augmentation and film-cooling effectiveness, Uzol et al. [31] studied the aerodynamic aspects of the trailing-edge cooling. They investigated how cut back length and rib spacing affect the discharge coefficient at different free-stream Reynolds numbers.

For all configurations, they showed that the discharge behavior weakly depend on the Reynolds number. They also showed that as the spanwise rib-spacing gets smaller, the aerodynamic performance of the configuration gets better. In their following work [32], they looked into the flow field near the trailing edge closely to clarify the reasons of pressure loss characteristics. Besides, they tried to numerically model flow near the trailing edge to shed light into the details of the flow field that was not resolved by experimental capabilities. They observed that for the ejection rates of 0 and 3, pressure loss levels were increasing while at the ejection rate 5, loss levels were reduced. Their computational results showed that the loss mechanisms were mainly ruled by the shear generated between the coolant and the mainstream.

Most of the research related to the trailing-edge cutback cooling are experimental. But, as in [32] there have been other attempts to numerically model the flow near the trailing edge. Holloway et al. [33] conducted experiments to see the unusual phenomenon related to the effect of increasing the blowing ratio on the film-cooling effectiveness and modeled the experimental set up numerically to look at the reasons of this phenomenon closely. Their experimental results showed that the effectiveness increases until blowing ratio 0.8 but it decreases between 1.0 and 1.25. Further increasing blowing ratio results in an increase in the effectiveness levels. They modeled the experiment using steady Reynolds Averaged Navier Stokes with RNG $k-\epsilon$ turbulence model. The computationally-calculated efficiency monotonically increases as the blowing ratio increases, which was not the case in the experiments. Their conclusion about that was that the unsteadiness in experiments could not be modeled using steady RANS, and an unsteady simulation was needed. In this direction, in their subsequent study [34] they focused on the unsteady modeling. Those results revealed that the interaction between the coolant and the mainstream vortices is responsible for the phenomenon observed in the first part of the study. Until a blowing ratio of 1, the mainstream vortices were dominant, but after that point the coolant vortex shedding became dominant, and they had approximately an equal strength near the blowing ratio of 1.

As is summarized in this chapter, there are many studies that investigate the coolant flow through a trailing edge slot geometry from a thermal performance perspective, while only a limited number of studies have been concerned with the aerodynamic

aspects. Among those limited studies, mostly circular pins have been of interest, while studies on other shapes have been much less in number. In this study, the effect of internal pin-array structures on the downstream trailing edge slot exit flow is investigated. Different pin shapes that are of circular, elliptical, and airfoil shape (NACA 0033 profile) with varying sizes are modeled, presenting a detailed comparison. The same airfoil shape is adopted with that of the island blockage of the trailing edge configuration, resulting in a unique pin-array and blockage combination that has not been investigated before according to the literature search performed during this thesis work. The results obtained in the internal cooling structure provide the inlet coolant profiles to the external cooling structure that consists of the pressure-side cut-back slot region. The downstream effects of the internal pin-array configurations are also examined in detail providing information on the slot film-cooling performance. Resulting internal and external flow field characteristics are investigated both from aerodynamic and thermal aspects of trailing edge design.

CHAPTER 3

METHODOLOGY

In this chapter, the computational method applied in the thesis is explained in detail. First, the mathematical modeling and numerical modeling approaches are defined. Then, the cases used for the validation of the numerical model are described. Discretization of the computational domains and the boundary conditions used in numerical modeling are presented. Finally, the cases used for comparing different pin shapes are explained with their discretization and boundary conditions.

3.1 Mathematical Modeling

The behavior of fluid flow can be mathematically modeled using governing equations. The governing equations are obtained by applying the conservation of mass, conservation of momentum and conservation of energy principles on the domain of interest. The differential forms of these conservation equations are presented below:

Conservation of Mass

$$\frac{\partial \rho}{\partial t} + \frac{\partial(\rho U_i)}{\partial x_i} = 0 \quad (3.1)$$

Conservation of Momentum

$$\frac{\partial(\rho U_i)}{\partial t} + \frac{\partial(\rho U_j U_i)}{\partial x_j} = -\frac{\partial p}{\partial x_i} + \frac{\partial \tau_{ij}}{\partial x_j} \quad (3.2)$$

Conservation of Energy

$$\frac{\partial(\rho(h_{tot}))}{\partial t} - \frac{\partial p}{\partial t} + \frac{\partial(\rho U_i h_{tot})}{\partial x_i} = \frac{\partial(U_i \tau_{ij})}{\partial x_i} + \frac{\partial(\lambda \frac{\partial T}{\partial x_j})}{\partial x_j} \quad (3.3)$$

3.2 Numerical Modeling

The analytical solutions of coupled governing equations exist for some simple cases. For solving the flow field of complex flow cases, numerical methods are developed. Mostly-used numerical approaches are the finite difference, finite volume, finite element, and spectral methods. The common property of numerical methods is that the differential forms of the governing equations are discretized and approximated as algebraic equations that can be solved computationally. To apply discretization methods on the flow domain, firstly the physical flow space need to be divided into small parts called grids. Scales of grids depend on the smallest length scales present in the flow domain. The smallest grid should be smaller than the smallest length scale of flow so that the flow field is fully resolved. This requirement becomes a problem according to the available computational power, especially for high Reynolds flows since the length scale gets smaller as Reynolds Number is increased.

Thanks to high performance of modern supercomputers, a direct solution of the discretized governing equations are possible for simple flows with Reynolds numbers up to order 10^5 . This method is called Direct Numerical Simulation (DNS) and it gives the most accurate results related to the flow domain. Other than DNS, to predict the effects of turbulence with less computational effort, different turbulence models were developed. In these methods, flow field variables are divided into average and fluctuating parts, and governing equations are reconstructed with average and time-dependent values. This method is called Reynolds Averaging. The related Reynolds-Averaged Navier-Stokes (RANS) equations are presented below:

$$\frac{\partial \rho}{\partial t} + \frac{\partial(\rho U_i)}{\partial x_i} = 0 \quad (3.4)$$

$$\frac{\partial(\rho U_i)}{\partial t} + \frac{\partial(\rho U_j U_i)}{\partial x_j} = -\frac{\partial p}{\partial x_i} + \frac{\partial(\tau_{ij} - \rho \overline{u_i u_j})}{\partial x_j} \quad (3.5)$$

$$\frac{\partial(\rho h_{tot})}{\partial t} - \frac{\partial p}{\partial t} + \frac{\partial(\rho U_j h_{tot})}{\partial x_j} = \frac{\partial(U_i(\tau_{ij} - \rho \overline{u_i u_j}))}{\partial x_i} + \frac{\partial(\lambda \frac{\partial T}{\partial x_j} - \rho \overline{u_j h})}{\partial x_j} \quad (3.6)$$

RANS equations contain additional flux terms. These are Reynolds stresses $\overline{\rho u_i u_j}$ and Reynolds fluxes $\overline{\rho u_j h}$. Reynolds stresses and fluxes contain fluctuating velocity components that are unknowns, which means that Reynolds-Averaging brings additional unknowns to the closed system of equations formed by Navier-Stokes equations. This problem is referred to as the "Closure Problem" in fluid dynamics. To overcome this problem, additional terms have to be modeled. Modeling of turbulence is an active research area and a large variety of turbulence models were developed. Main categories of turbulence models are first order closures, second order closures, and Large Eddy Simulation.

In this work for numerical modeling, a commercial software ANSYS CFX was used and the fluid flow was modeled using the 3D Reynolds-Averaged Navier-Stokes (RANS) equations. For discretization, CFX uses a dual median finite-volume method. A high-resolution advection scheme was used for evaluating the discretized equations. Formulation of scheme is given in equation 3.7 where φ means any scalar variable. Integration point value of variable is calculated using upwind node value (φ_{upw}), control volume gradient of variable φ ($\nabla\varphi$), vector between integration point and upwind node ($\Delta\vec{r}$), and flux limiter parameter β . This scheme switches from the second order to the first order depending on the value of β . This parameter changes between 0 and 1 according to the boundedness principle described by Barth and Jespersen [35]. The methodology is explained via the equations 3.8, 3.9, and 3.10. Application of this method requires the computation of minimum and maximum values of φ in the upwind node and its adjacent nodes. Since the integration point value should be between the minimum and maximum values, to eliminate overestimation or underestimation, the β formulation given in equation 3.10 is used.

$$\varphi_{ip} = \varphi_{upw} + \beta \nabla\varphi \Delta\vec{r} \quad (3.7)$$

$$\varphi_i^{max} = \max\{\varphi_{upw}, \varphi_i^{max}\} \text{ and } \varphi_i^{min} = \min\{\varphi_{upw}, \varphi_i^{min}\} \quad (3.8)$$

$$\varphi_i^{min} < \varphi_{ip} < \varphi_i^{max}, \forall i \quad (3.9)$$

$$\beta = \min_{\forall i} \begin{cases} \min\{1, \frac{\varphi_i^{max} - \varphi_{upw}}{\varphi_i - \varphi_{upw}}\} & \varphi_i - \varphi_{upw} > 0 \\ 1 & \varphi_i - \varphi_{upw} = 0 \\ \min\{1, \frac{\varphi_i^{min} - \varphi_{upw}}{\varphi_i - \varphi_{upw}}\} & \varphi_i - \varphi_{upw} < 0 \end{cases} \quad (3.10)$$

To satisfy closure, the Reynolds stresses are modeled using the $k - \omega$ based Shear Stress Transport (SST) [36] that is a two-equation Eddy Viscosity turbulence model. This model behaves like the $k - \epsilon$ model outside of the boundary layer and the $k - \omega$ model inside of the boundary layer with the help of the blending function. Additionally, in order to restrain the over-prediction of eddy-viscosity, a limiter was used in its formulation. For this model Eddy Viscosity is formulated with blending function F_2 and magnitude of strain rate tensor S_{ij} as follows:

$$\nu_t = \frac{5/9k}{\max(5/9\omega, SF_2)} \quad (3.11)$$

$$F_2 = \tanh([\max(\frac{2\sqrt{k}}{0.009\omega y}, \frac{500\nu}{y^2\omega})]^2) \quad (3.12)$$

$$S = \sqrt{2S_{ij}S_{ij}} \quad (3.13)$$

Since the use of wall function is not encouraged for the separated and recirculating flows, the automatic wall function provided by CFX for the $k - \omega$ based models was active. This wall function automatically switches from a low-Reynolds to a near-wall formulation when the boundary layer is highly resolved [37]. In this method specific dissipation rate ω and friction velocity u_τ formulated combining both viscous sub-layer and logarithmic region formulations. Their formulations are given in equations below where Δy is THE wall normal distance between the first and the second nodes.

$$u_\tau^{vis} = \sqrt{\frac{\mu}{\rho} \left| \frac{\Delta U}{\Delta y} \right|} \quad (3.14)$$

$$u_\tau^{log} = \frac{U}{1/\kappa \ln\left(\frac{\sqrt{\frac{\tau_w}{\rho}} \Delta y}{\nu}\right) + c} \quad (3.15)$$

$$u_\tau = \sqrt[4]{(u_\tau^{vis})^4 + (u_\tau^{log})^4} \quad (3.16)$$

$$\omega_{vis} = \frac{6\nu}{0.075(\Delta y)^2} \quad (3.17)$$

$$\omega_{log} = \frac{\sqrt{(u_\tau^{vis})^4 + (\sqrt{0.3k})^4}}{0.3\kappa\Delta y\sqrt{\frac{\tau_w}{\rho}}} \quad (3.18)$$

$$\omega_\omega = \omega_{vis}\sqrt{1 + \left(\frac{\omega_{log}}{\omega_{vis}}\right)^2} \quad (3.19)$$

3.3 Validation Case

Validation case selected for this study is taken from the experimental study of Ling et al. [3]. Magnetic resonance imaging is used for measuring the 3D velocity field and the coolant concentration fields at the downstream of the trailing edge pressure-side film-cooling slots. NACA-0012 airfoil with 283 mm blunted trailing edge chord and 76 mm span are used in the experiments. Inner section of the airfoil includes a coolant channel with four rows of pin fins and NACA-0033 profile shaped blockages. Last 42.1 mm of the blade is cut out from the pressure side and is stiffened with 7 mm-wide lands. The coolant flows through the breakout surface from the slots with 5 mm height and 17 mm length. The details of the geometry are given in Figure 3.1.

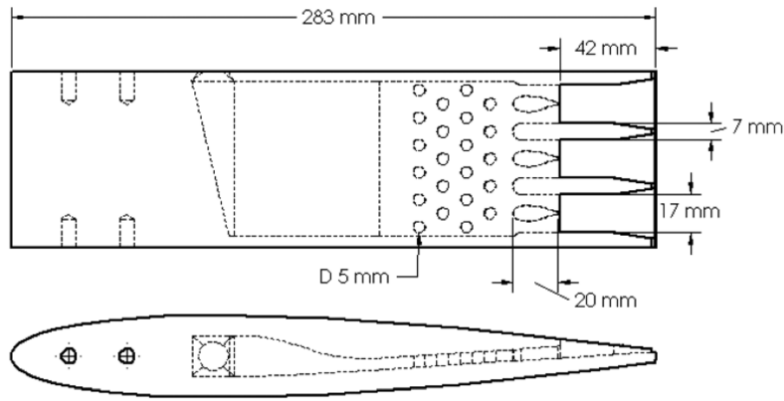
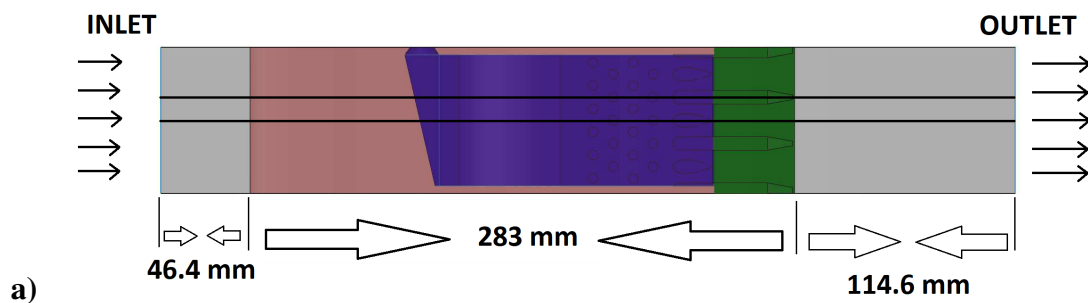
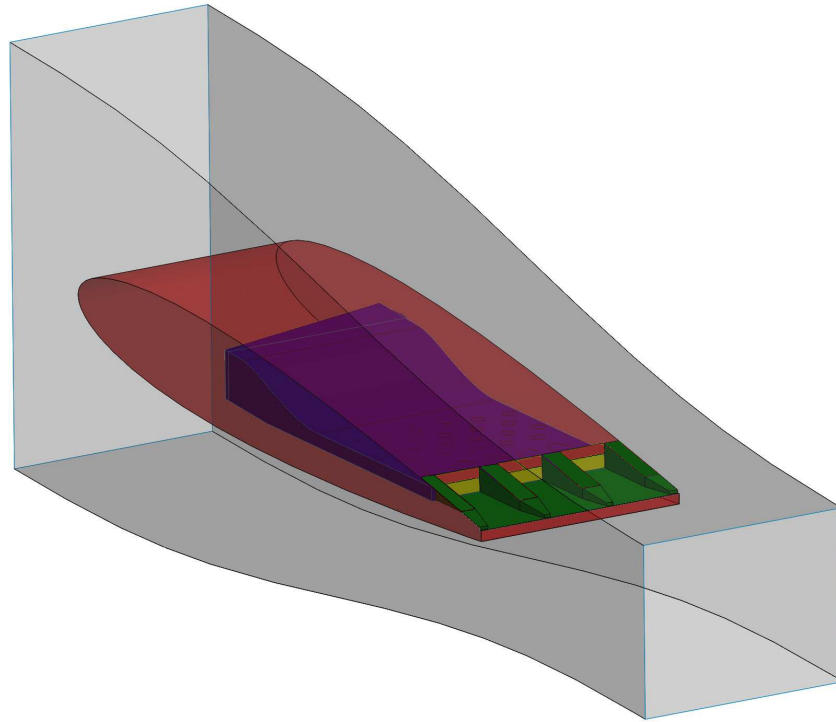


Figure 3.1: Schematic Of Experimental Model [3]

The validation case is divided into two parts for this work. First, the flow inside the cooling channel is investigated. Then, by using the results of the cooling channel, the external film cooling part that includes the trailing-edge breakout surface is investigated. For the first part, the whole cooling channel from the coolant inlet to the slot exit is modeled. Internal section model is shown as blue in Figure 3.2. Results of the first part showed relatively uniform flow for all three slots and this situation is observed in the experiments as Ling et al. [1] mentioned. Due to the symmetry of the geometry and the uniformity of the flow structure at the slot exit, the symmetry boundary conditions were imposed for the external cooling validation. The flow domain that includes the half of the slot and half of the land is modeled for the second part. The modeled slot and land geometry is shown between two solid lines in part (a) of Figure 3.2. The region of interest for external and internal cooling is shown with green and purple colors respectively, while the yellow region in part (b) of Figure 3.2. is a common part of the solution domains for the internal and external validation cases.





b)

Figure 3.2: Schematic Of Validation Model a) Top View , b) Isometric View

3.3.1 Internal Cooling

3.3.1.1 Boundary Conditions

Boundary conditions of the numerical model is set to match with those of the experiments of Ling et al. [1]. The typical velocity-inlet and static pressure-outlet type of boundary conditions were applied on the model. The details of the experiment include mostly the main flow inlet conditions and the turbulence intensity, but there is no information about the coolant flow conditions at the coolant inlet. For this reason, the inlet velocity is determined through iterations so that the average coolant velocity at the slot exit and the coolant mass flow rate given in Table 3.1 are matched with that of the experiment. There was no explanation about the coolant inlet turbulence characteristics and the velocity profile. However, in Ling et al. [1]’s computational work, it is observed that the predictions were insensitive to the coolant inlet conditions [1]. Regarding this observation, inlet velocity is taken to be uniform and the turbulence

intensity was assumed to be 5% for the computations. The end walls, pins, slots, and the airfoil-shaped blockages were modeled with no-slip and fixed temperature surfaces.

Table 3.1: Experimental Conditions From Ref [1]

Average Bulk Velocity at Slot Exit [m/s]	0.39
Average Coolant Velocity at Slot Exit [m/s]	0.30
Coolant Temperature [$^{\circ}\text{C}$]	20
Working Fluid Density [kg/m^3]	998
Coolant Mass Flow Rate [l/min]	4.41

The coolant used in the experiments is water. In the experiments, copper sulfate is mixed with water to enhance signal to noise ratio and effectively use MRV. Density and viscosity of used solution are negligibly different than pure water. Because of this reason, in this work coolant is used as pure water. The fluid domain is modeled as a constant-property pure water at 1 atm reference pressure and at 25°C reference temperature with a specific heat capacity of $4181.7 \text{ J}/\text{kg}\cdot\text{K}$ at constant pressure and a dynamic viscosity of $8.899 \times 10^{-4} \text{ kg}/\text{m}\cdot\text{s}$.

3.3.1.2 Geometry and Meshing

A schematic of the flow domain used in the internal cooling validation study is shown in Figure 3.3. Coolant enters the domain through a circular opening on the side and the triangle-shaped domain turns the flow through the pins. Coolant leaves the domain through the slots located downstream of the airfoil-shaped blockages.

The computational domain was meshed using ICEM CFD software. Due to the complexity of the geometry, the domain was discretized using tetrahedral elements. Prism elements were used around the pins, airfoil-shaped blockages, slots, and at the end walls. The thickness of the first prism cells were selected such that maximum y^+ is equal to 1. This is recommended for accurate heat transfer predictions [37]. To satisfy this, near-wall spacing was set as 0.006 mm. The growth of prism layers was set as exponential with constant rate of 1.2. 19 prism elements are used to represent

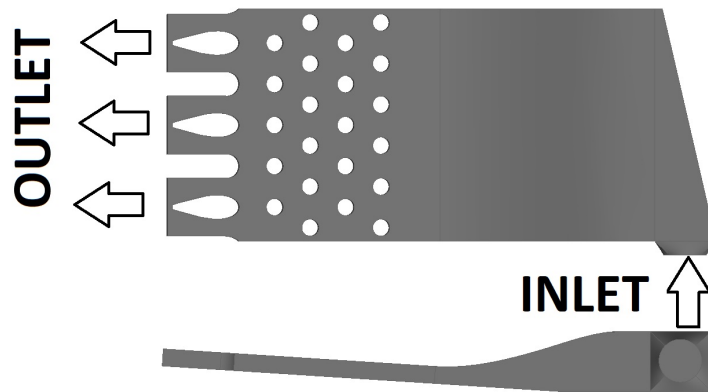
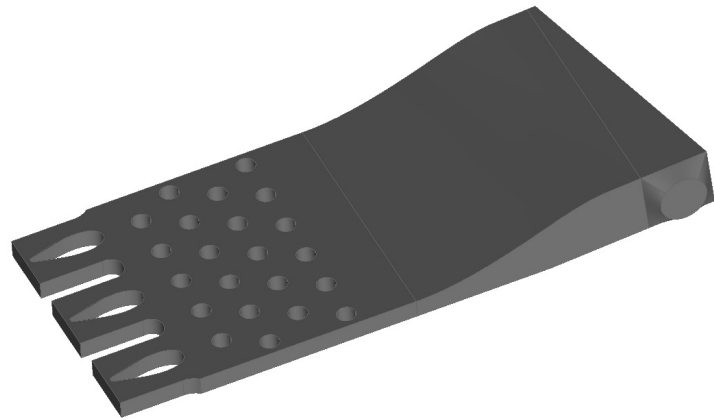


Figure 3.3: Computational Domain Used For Internal Validation Case

the boundary layer. Figure 3.4 shows the grid used in validation study and zoomed-in view which includes the last row of pins and the trailing edge exit region with a land and a blockage.

A grid sensitivity study was conducted by using different sizes of three grids with the number of elements varying from 1.1M to 5.6M. The sensitivity study was performed by monitoring the velocity profiles along the centerline of the pin array across the top and bottom walls of the computational domain. Figure 3.5 shows the velocity profiles along the centerline for three different grid solutions.

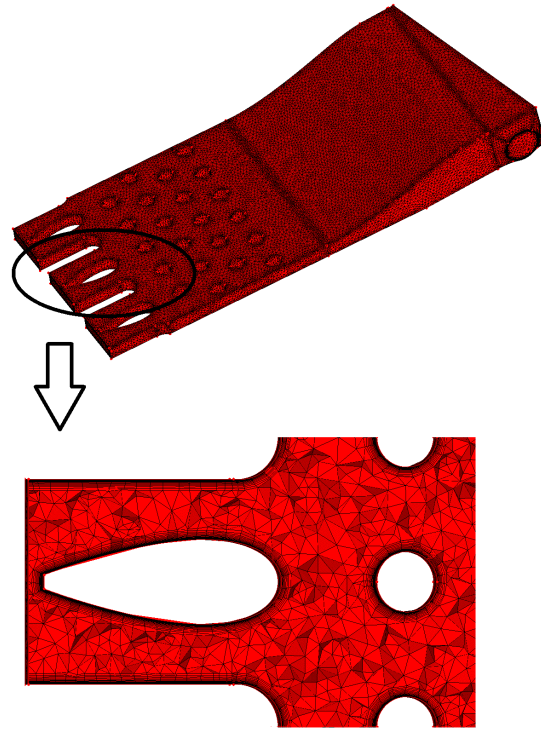


Figure 3.4: Meshing Used For Internal Validation Case

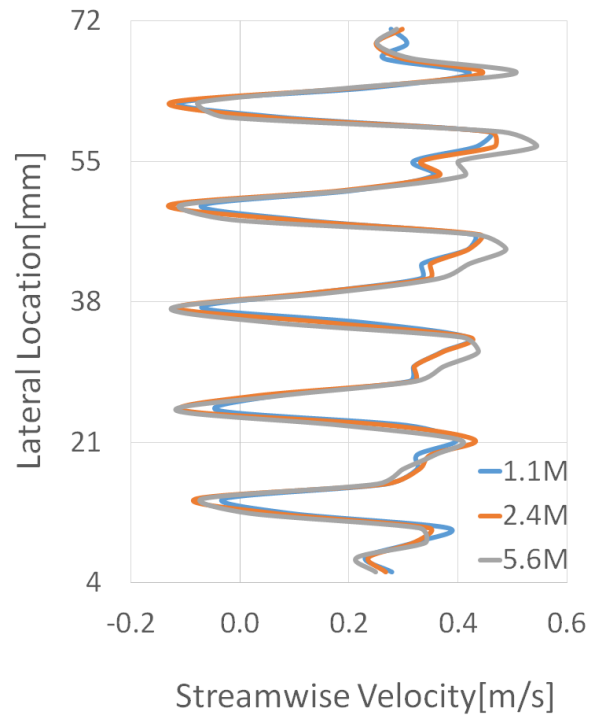


Figure 3.5: Streamwise Velocity Profiles For Internal Validation Case Grid Sensitivity Study

The average percentage of differences between coarser, medium and finer grids were calculated by using Equation 3.20 where ζ_{finer}^i is the solution of finer grid and ζ^i is the solution of the grid of interest at the i^{th} data point and N is the total number of data points.

$$Average \% Difference = \frac{\sum_{i=1}^N \frac{\zeta_{finer}^i - \zeta^i}{\zeta_{finer}^i}}{N} \quad (3.20)$$

The average percentage of differences between 1.1M and 2.4M was calculated as 11.3 % while 2.4M and 5.6M was calculated as 9.1 %. Due to the computational cost of further refinement, the grid with 2.4 M elements was selected for the validation study.

3.3.1.3 Solution Convergence

Figure 3.6 shows the convergence levels obtained.

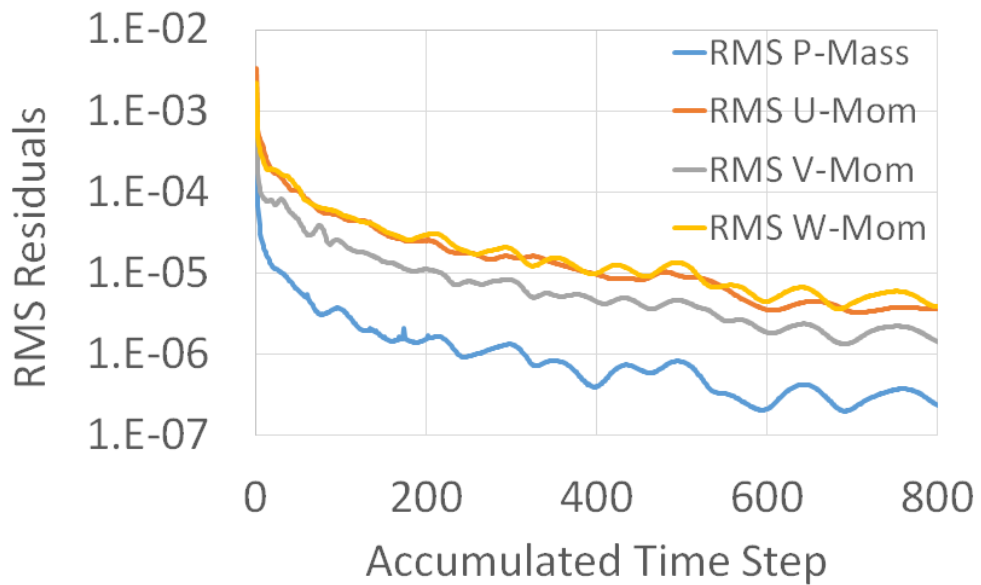


Figure 3.6: RMS Residuals For Internal Validation Case

3.3.2 External Cooling

3.3.2.1 Boundary Conditions

Boundary conditions of the numerical model is again set to match with those of the experiments of Ling et al. [1]. The typical velocity-inlet and static pressure-outlet type of boundary conditions were applied on the model. The slot region is modeled as an opening and the velocity profile information is imported from the results of the internal cooling validation part. In the internal cooling part, the slot region boundary condition was set as atmospheric pressure. To be consistent with the internal cooling part, outlet pressure in external cooling part is adjusted to give atmospheric pressure at the slot region. Since the fluid used is water at low velocity, setting the outlet static pressure to match the atmospheric pressure gave only 0.02 % difference in the slot static pressure, which is considered to be negligible.

Table 3.2: External Flow Experimental Conditions From Ref [1]

Main Flow Inlet Velocity[m/s]	0.19
Inlet Turbulence Intensity[%]	1
Inlet Turbulent Length Scale [mm]	1
Main Flow Temperature [⁰ C]	20
Main Flow Mass Flow Rate[l/min]	123

3.3.2.2 Geometry and Meshing

A schematic of the flow domain used in the external cooling validation study and the domain names are shown in Figure 3.7. Coordinates of the test section and the dimensions of the blade are taken from Ling et al. [1]. Main flow enters the domain through the inlet and the coolant enters the domain through the section named as blowing area. This presented domain is the outlet of the internal validation case.

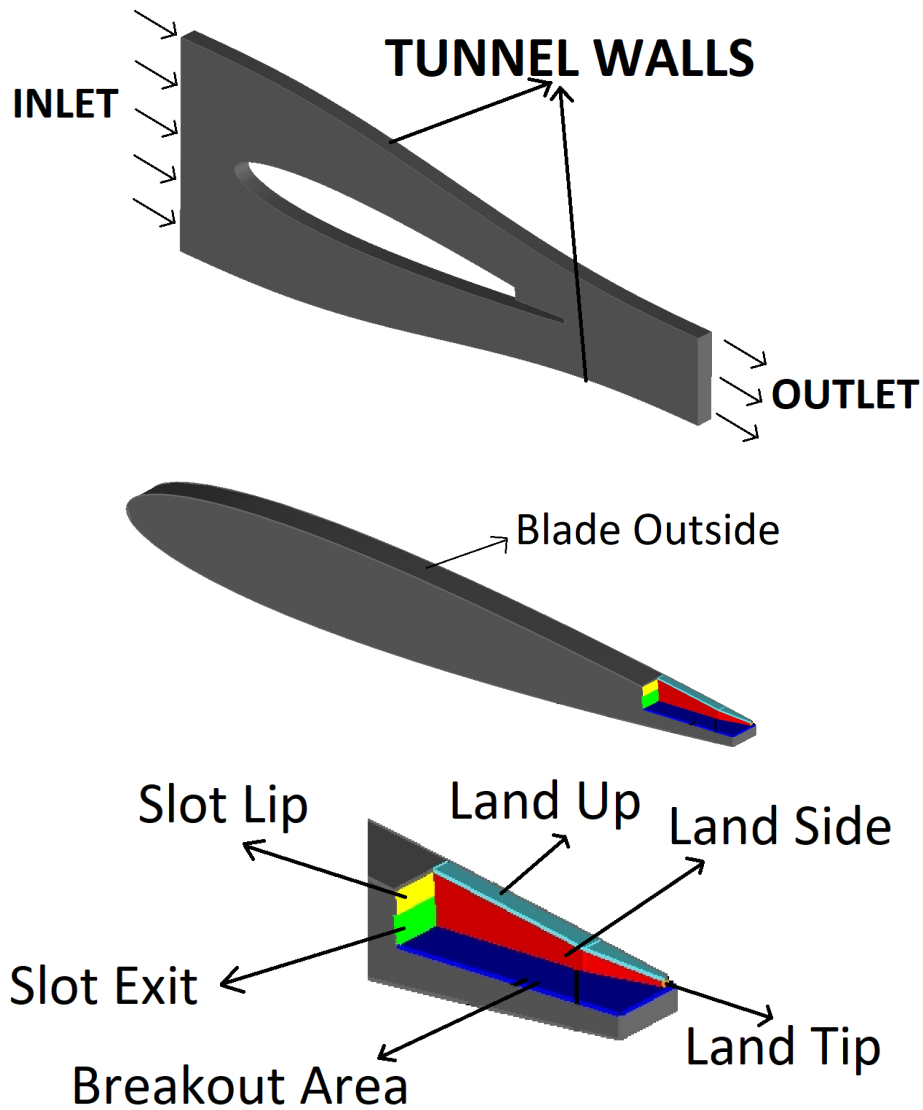


Figure 3.7: Computational Domain Used For External Validation Case

The main flow inlet was placed 46.4 mm slot-height upstream of the blade leading edge and the outlet was placed 114.6 mm slot-height downstream of the blade trailing edge. To take advantage of symmetry and to decrease computational effort, only half of the slot and half of the land are included in this validation study.

For meshing, the domain is discretized using unstructured tetrahedral elements and prism elements are used in near-wall regions. First layer thicknesses around the walls are adjusted so that y^+ is kept around 1. It is proved that the tetrahedral mesh with

prism layers for capturing the boundary layer can be used in order to predict laterally-averaged film effectiveness downstream of the coolant holes [38]. Since outer domain is not far from the blade, prism elements are used for tunnel walls, too. Since the main flow and the coolant are mixing downstream of the slot, the density of the grid is increased in that region. Figure 3.8 shows the external geometry meshing and a close-up look of the slot region.

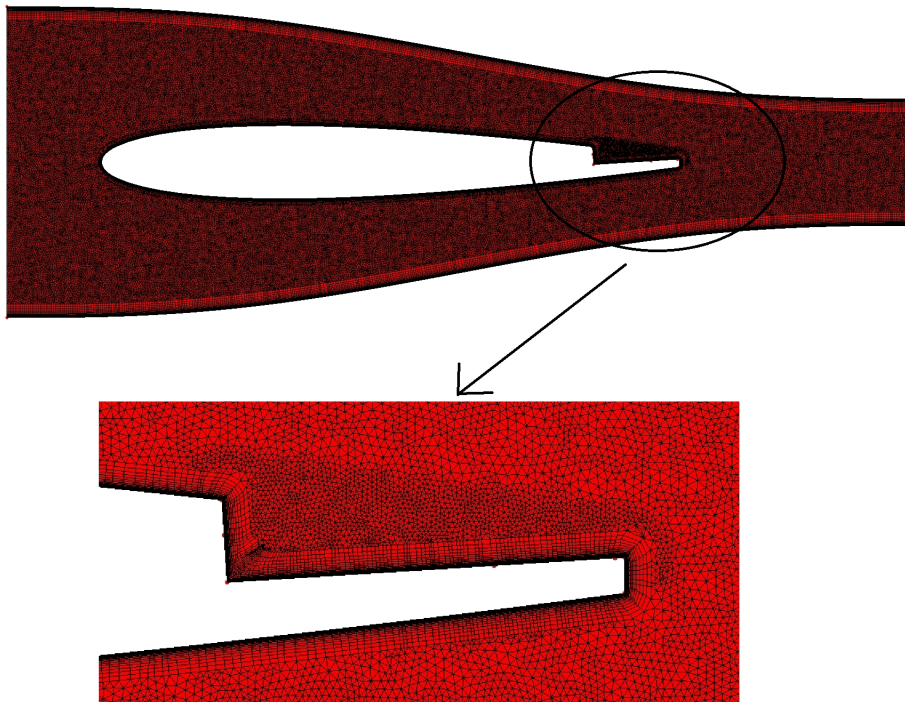


Figure 3.8: Grid Used In External Validation Case

To satisfy y^+ around 1, near wall spacing was set as 0.022 mm around the blade, slot, and the land region, and 0.035 mm around the tunnel walls. The growth of the prism layers was set as exponential with constant rate of 1.2. 20 layers for tunnel walls and 18 layers for other walls were implemented. For grid sensitivity, prism layer parameters are kept constant. This study was performed for the grids with 1.3 M, 3.8 M and 8.4 M elements. The methodology explained in Section 3.3.1.2 is applied. Streamwise velocity profiles on the mid section of the plane 2.5 mm above the breakout region are presented in Figure 3.9. This location is selected since the region of interest in this study is the breakout region. According to these results, the

grid with 3.8 M elements were selected since the average percentage of the difference between the medium and the fine mesh is 2.1% while the difference between the coarse and the medium mesh is 1.5%.

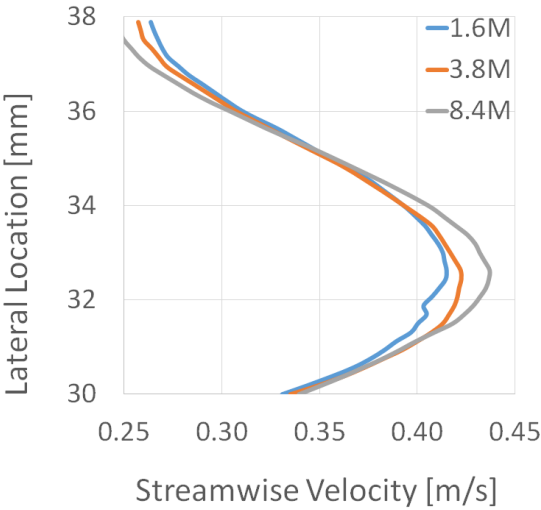


Figure 3.9: Streamwise Velocity Profiles For External Validation Case Grid Sensitivity Study

3.3.2.3 Solution Convergence

Figure 3.10 shows the convergence levels obtained.

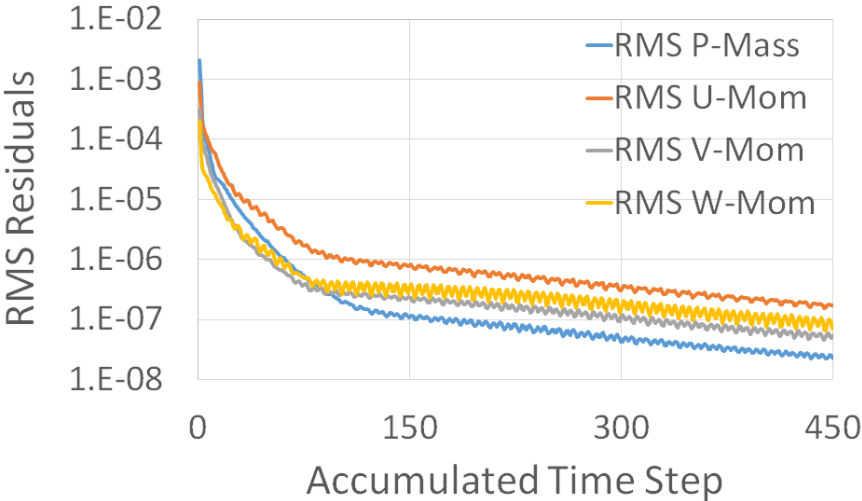


Figure 3.10: RMS Residuals For External Validation Case

3.4 Comparison Cases

For the comparative studies, five different cases are prepared. In the internal cooling part, the aerothermodynamic performances of three different pin shapes that are of circular, elliptic, and NACA-0033 profile airfoil are investigated. Besides, in order to see the effect of pin size, smaller-sized elliptic and airfoil-shaped pins are analyzed. In the external cooling part, the film-cooling performances of different pin shapes using the results from the internal cooling part are investigated.

3.4.1 Internal Cooling

3.4.1.1 Boundary Conditions

For comparison cases, the boundary conditions are taken from the experimental measurements that were obtained by Hylton et al. [39] for the C3X cascade vane. The boundary conditions are different from the validation case. This change is necessary since the validation case is performed with water and with conditions that do not represent the real engine environment. In their study, Benson et al. [40], who performed experiments at the same test facility with the same basic flow configuration as the validation case, concluded that even if the Reynolds number range that was tested with water was significantly less than that in real engine environment, it represented a fully turbulent flow where the main flow characteristics were not significantly affected with an increase in Reynolds number. Therefore, this agreement obtained between predictions and data provides a validation for the subsequent comparative studies that were performed with air as an ideal gas.

The computations are performed for the selected boundary conditions that reflect the actual engine operation conditions. The experimental data sets presented in [39] contain various parameters like total temperature, total pressure, Mach number, Reynolds number, wall-to-gas temperature ratio at various locations. Cases 4421 and 4422 are selected for this study. The necessary boundary conditions to perform the computations were either adopted directly from [39] or were calculated if they were not readily available. A summary of these conditions is given in Table 3.3. The coolant

inlet velocity is calculated using the main inlet conditions such that the blowing ratio is equal to 0.8 as a typical value. The coolant inlet velocity was taken to be uniform. The inlet turbulence intensity was kept at 5% as in the validation case. All solid walls were modeled using the no-slip boundary conditions with a constant temperature of approximately 614 K . The approach for thermal boundary conditions are taken from [18]. The fluid domain is modeled as a calorically perfect ideal gas with a specific heat capacity of 1004.4 $J/kg.K$ at constant pressure and a dynamic viscosity of $1.831 \times 10^{-5} \text{ kg/m.s}$.

Table 3.3: Internal Flow Comparison Case Boundary Conditions

Coolant Inlet Velocity[m/s]	31.1
Coolant Inlet Temperature[K]	478.2
Wall Temperatures [K]	614.2
Outlet Static Pressure [kPa]	332.1

3.4.1.2 Geometry and Meshing

For comparisons, the internal-cooling validation domain is simplified and the coolant flow is introduced into the passage directly in the streamwise direction. This made it possible to reduce the size of the computational domain as the flow through the trailing edge internal geometry becomes symmetrical in addition to the symmetry of the geometry itself. Using a plane of symmetry through the centerline of the model, the grid size was halved. This simplification was justified by experiments [1]. In the experiments the coolant was fed into the domain radially and the pin-fin geometry orients the flow uniformly at the slot exit. Since this work considers only the geometric section of the pin-array, the coolant was fed directly in the streamwise direction to the domain.

The reference pin shape used is circular and it has 5 mm diameter. Elliptical and airfoil-shaped pins are sized such that the minor axes of the elliptical pins and the maximum thicknesses of the airfoil-shaped pins have the length of a circular pin diameter. This way, frontal areas of all shapes were kept the same rather than their circumferences, as was done in [14], guaranteeing the same amount of flow blockage

Table 3.4: Internal Comparison Case Model Dimensions

Streamwise Length [mm]	79.82
Height [mm]	5.00
Diameter of Circular Pins [mm]	5.00
Major Axis Length of Elliptical Pins [mm]	14.07
Chord of Airfoil-Shaped Pins [mm]	14.07
Minor Axis Length of Small Elliptical Pins [mm]	1.78
Maximum Thickness Length of Airfoil-Shaped Pins [mm]	1.78

area. Major axis length of the elliptical pins is selected such that it is the same as the chord of the airfoil-shaped pin. To see the size effect, small elliptical and small airfoil-shaped pins are created such that the major axis of elliptical pin and the chord of the airfoil-shaped pin are equal to the diameter of the circular pin. The major axis-to-minor axis ratio of the small elliptical pins is matched to that of the larger elliptical pins.

The dimensions of the models used in the comparative study are summarized in Table 3.4. The base model is a constant 5 mm-height-section that has a 79.82 mm-streamwise length. The inlet of the domain coincides with the end of the smooth contraction from the coolant inlet into the constant-height pin section. Four rows of pin fins are placed along the section, with straight lands and airfoil-shaped blockages at the end of the section. An airfoil shape is used for the benefit of separation reduction in the wake. The flow domains used in the internal cooling comparison study is shown in Figure 3.11.

Similar to the validation studies, the prism elements were used around the pins, airfoil-shaped blockages, slots, and at the end walls. The thickness of the first prism cells were selected such that the maximum y^+ is equal to 1. To satisfy this, near wall spacing was set as 0.0008 mm. The growth of prism layers were set as exponential with constant rate of 1.2, and 30 prism elements are used to refine the boundary-layer region.

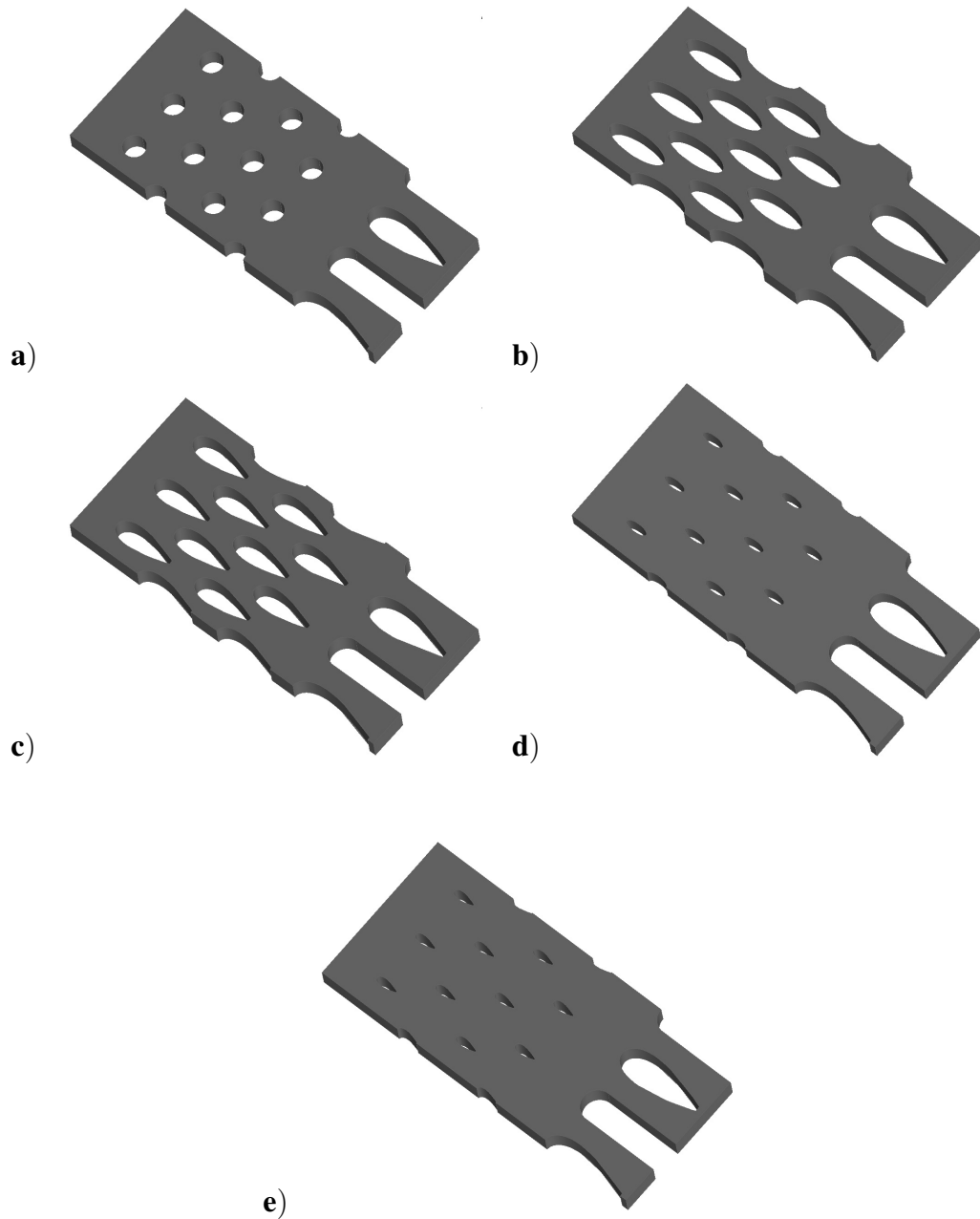


Figure 3.11: Computational Models Used In Internal Comparative Study a) Circular, b) Elliptical, c) Airfoil Shaped, d) Small-Elliptical, e) Small-Airfoil Shaped

A grid sensitivity study is performed as explained in Section 3.3.1.2 for the grids with 650 K, 1.6 M and 3.4 M elements. Figure 3.12 shows the streamwise velocity profiles along the centerline of the pin array across the top and bottom walls of the computational domain. The average percentage of the difference between the coarse and the medium grid was observed to be 9.7%, and the difference between the medium

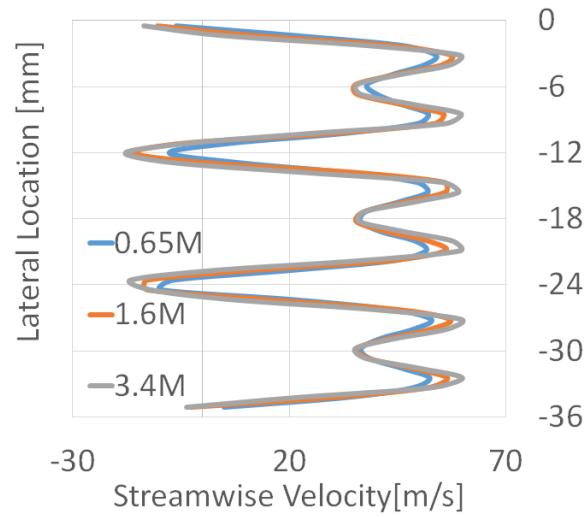


Figure 3.12: Streamwise Velocity Profiles For Internal Comparison Case Grid Sensitivity Study

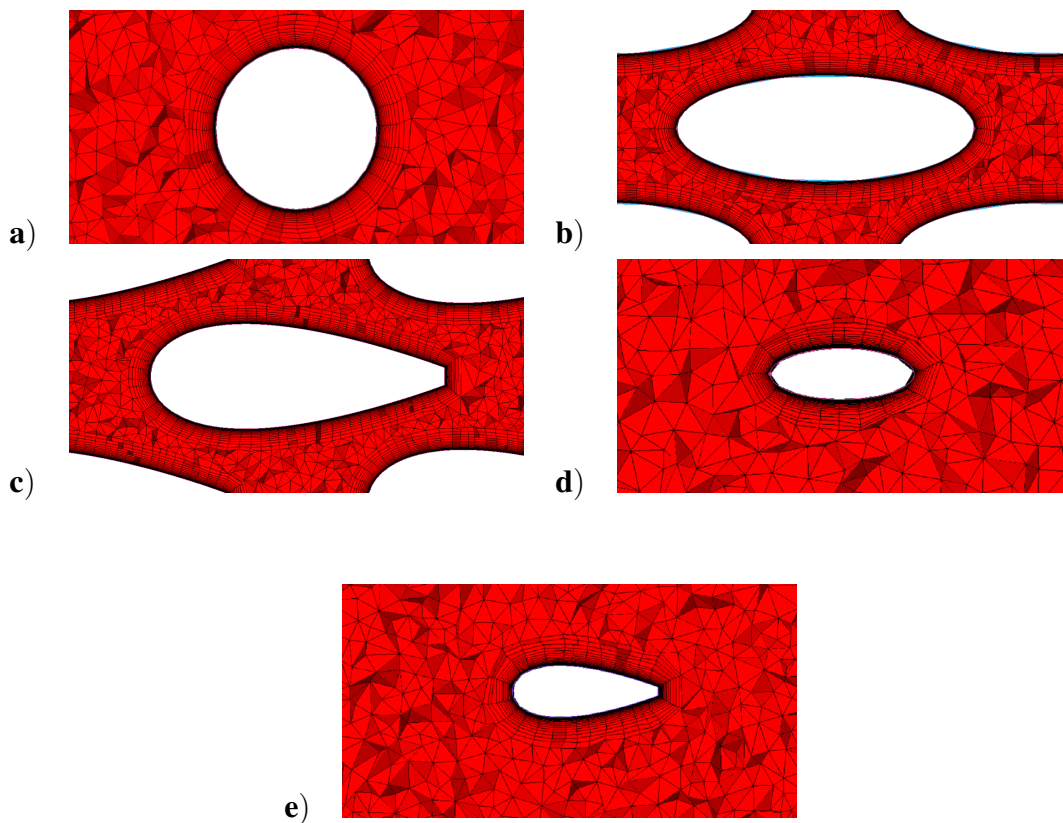


Figure 3.13: Near-pin Location Zoomed-in Views Of Grids Used In Comparative Study a) Circular, b) Elliptical, c) Airfoil Shaped, d) Small-Elliptical, e) Small-Airfoil Shaped

and the finer grid was observed to be 9.1% for the circular-pin case. As a result, the case with 1.6 millions of elements is decided to be used in the rest of the comparison study. Other configurations are meshed with the same parameters selected for the circular-pin geometry, and the corresponding grids of similar sizes are used for those cases. The mesh in the pin vicinity for each case is shown in Figure 3.13

3.4.1.3 Solution Convergence

Figure 3.14 shows the convergence levels obtained.

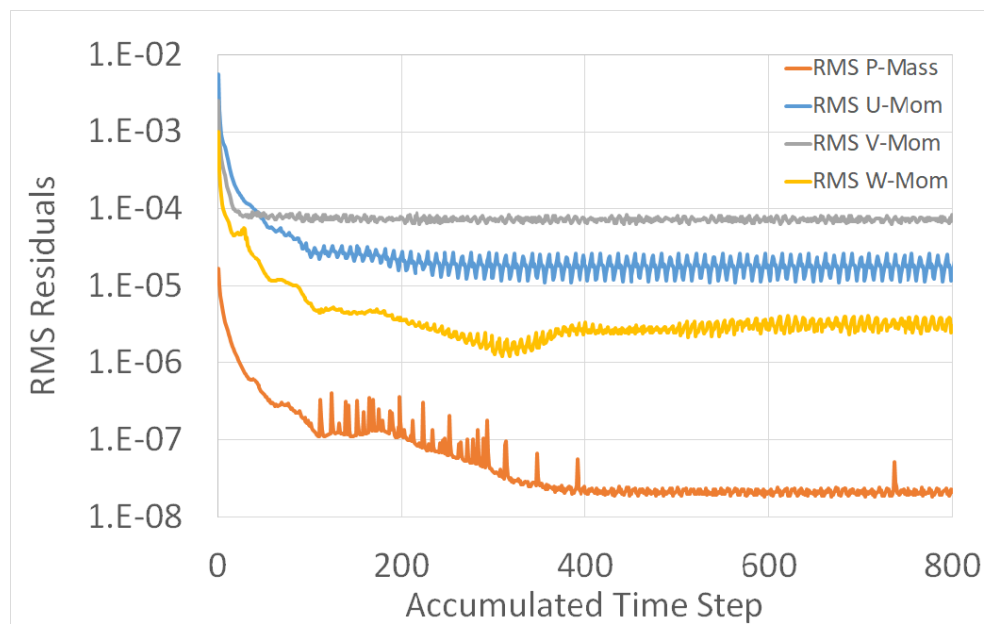


Figure 3.14: RMS Residuals For Internal Comparison Case

3.4.2 External Cooling

3.4.2.1 Boundary Conditions

For comparison cases, the boundary conditions are taken from the experimental measurements that were obtained by Hylton et al. [39] for the C3X cascade vane. The typical velocity-inlet and static pressure-outlet type of boundary conditions were applied on the model. The slot region is modeled as an opening. The velocity profile and the static temperature is used as the boundary condition at the blowing area. This

information is imported from the results of the comparison cases of internal cooling. Velocity profiles of different pin shapes are presented in Figure 3.15 and static temperatures are presented in Table 3.5.

Table 3.5: Mass Flow Averaged Slot Static Temperatures For Different Pin Shapes

Circular[K]	504.2
Elliptical[K]	505.5
Airfoil Shaped [K]	505.1
Small-Elliptical [K]	498.6
Small-Airfoil Shaped [K]	498.8

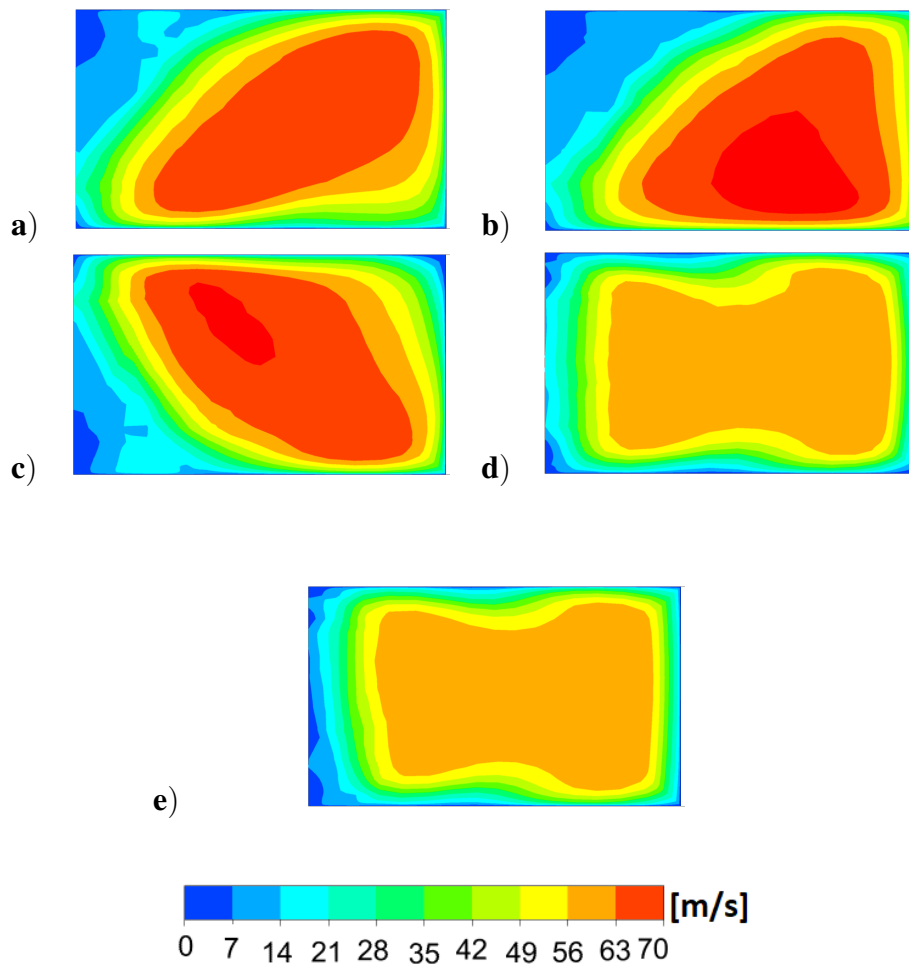


Figure 3.15: Blowing Area Velocity Profiles a) Circular, b) Elliptical, c) Airfoil Shaped, d) Small-Elliptical, e) Small-Airfoil Shaped

The inlet velocity is calculated as 95.32 m/s from the inlet Mach number given in the data set [39] and this same value is used for all five comparison cases. The inlet turbulence level is set as 8.3 % and inlet total temperature is set as 782 K. The outlet pressure is calibrated such that the average static pressure at the slot exit is equal to the boundary condition supplied at the internal comparison case, giving a value of 307.8 kPa. All solid walls are modeled using the no-slip boundary conditions and they are treated as adiabatic. The approach for thermal boundary conditions is taken from [18].

3.4.2.2 Geometry and Meshing

In the comparison study, the same airfoil and tunnel geometry presented in 3.3.2.2 are used. The only difference is that the slot region was connected to the breakout surface with a 3.6 degree-angle in the experimental setup and therefore this was mimicked in the validation case, but in the comparison case this angle is taken as zero.

The same meshing strategy explained in Section 3.3.2.2 is applied. First cell height of all walls are taken as 0.0011 mm. For the grid sensitivity study, meshes with 2.7 M, 6.0 M and 14.2 M elements are used. Figure 3.16 shows the streamwise velocity

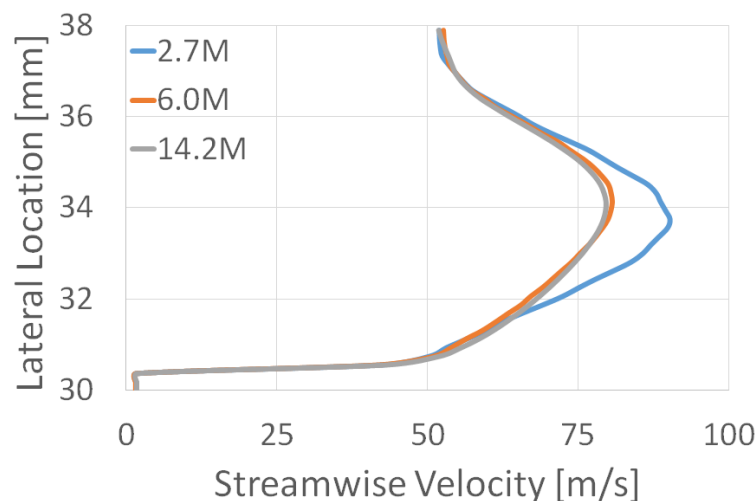


Figure 3.16: Streamwise Velocity Profiles For External Comparison Case Grid Sensitivity Study

profiles along the same line used for the external validation case that was previously described. The average percentage of the difference between the medium and the fine mesh is 1.7% and the difference between the coarse and the medium mesh is 5.2% . This is why the medium case with 6.0 M elements is selected for the external comparison study.

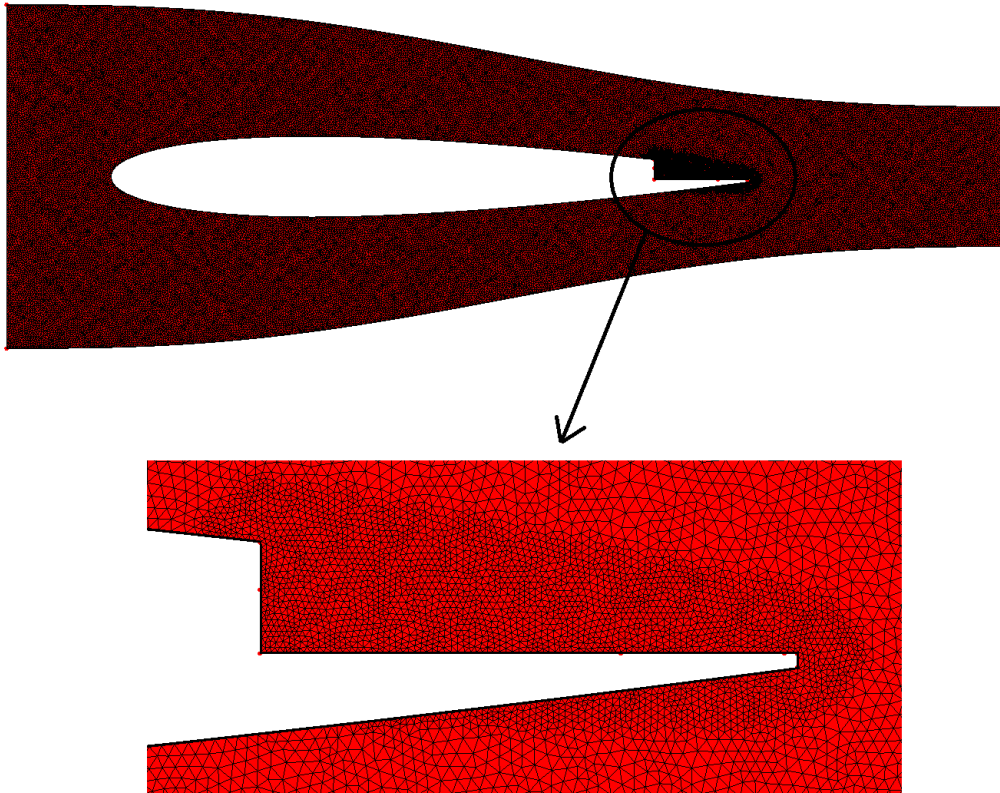


Figure 3.17: Grid Used In External Comparison Case

Figure 3.17 shows the external geometry meshing and a close-up look of the slot region. This mesh is used for all five comparison cases with the same meshing parameters.

3.4.2.3 Solution Convergence

Figure 3.18 shows the convergence levels obtained.

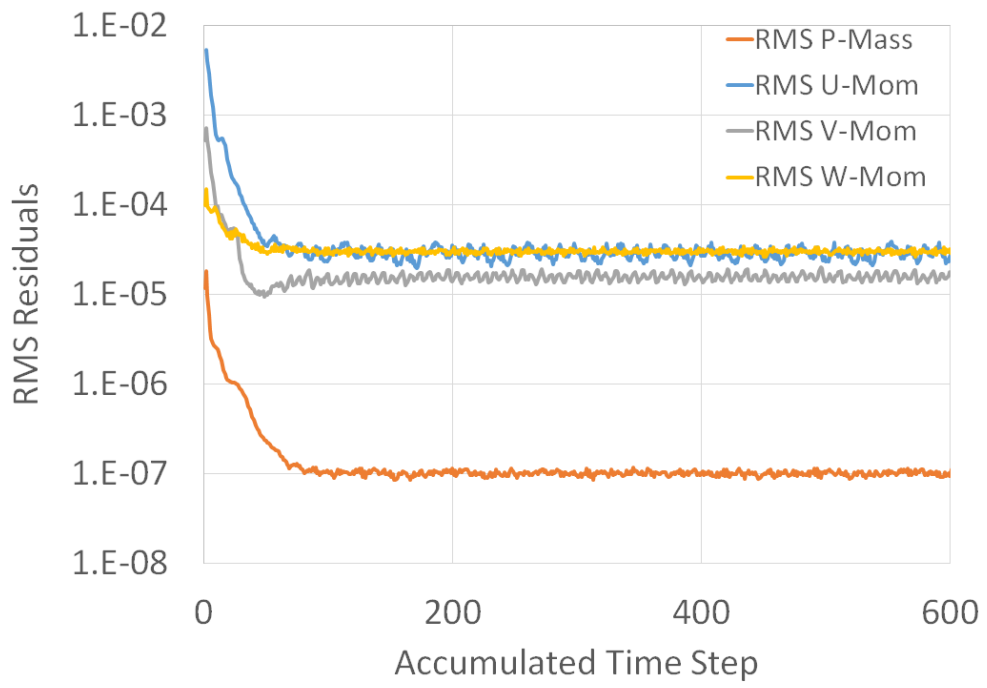


Figure 3.18: RMS Residuals For External Comparison Case

CHAPTER 4

INTERNAL COOLING ANALYSIS & RESULTS

In this chapter, the analysis performed and the results obtained in the internal cooling study are presented. First, the applied convergence criterion is explained. Then, the results for the validation study are shown and the validation of the model is presented. The comparison study results are divided into two parts as aerodynamic and thermal. The chapter is concluded with the comparison of aerodynamic and thermal performances of five different pin-fin geometries.

4.1 Validation

The comparison between the predictions and the experiment is shown in Figure 4.1 in the form of contours of streamwise velocity component through the pin arrays and the slot exit of the test configuration. The velocity is non-dimensionalized with the average experimental pressure-side main flow velocity, where u_{bulk} is given in Table 3.1, at the plane of the slot exit [3]. The contours are shown on a plane that is 2 mm above the bottom surface as was done by Ling et al.[3] for data demonstration. The non-dimensionalization method is given by Equation 4.1 where u_s is the local coolant velocity:

$$u_s' = \frac{u_s}{u_{bulk}} \quad (4.1)$$

Because the coolant is injected from the side of the domain at an upstream location, there is an observable asymmetry in the flow field entering the domain. Figure 4.1 presents the comparison in a portion of the domain demonstrated in Figure 3.3 where

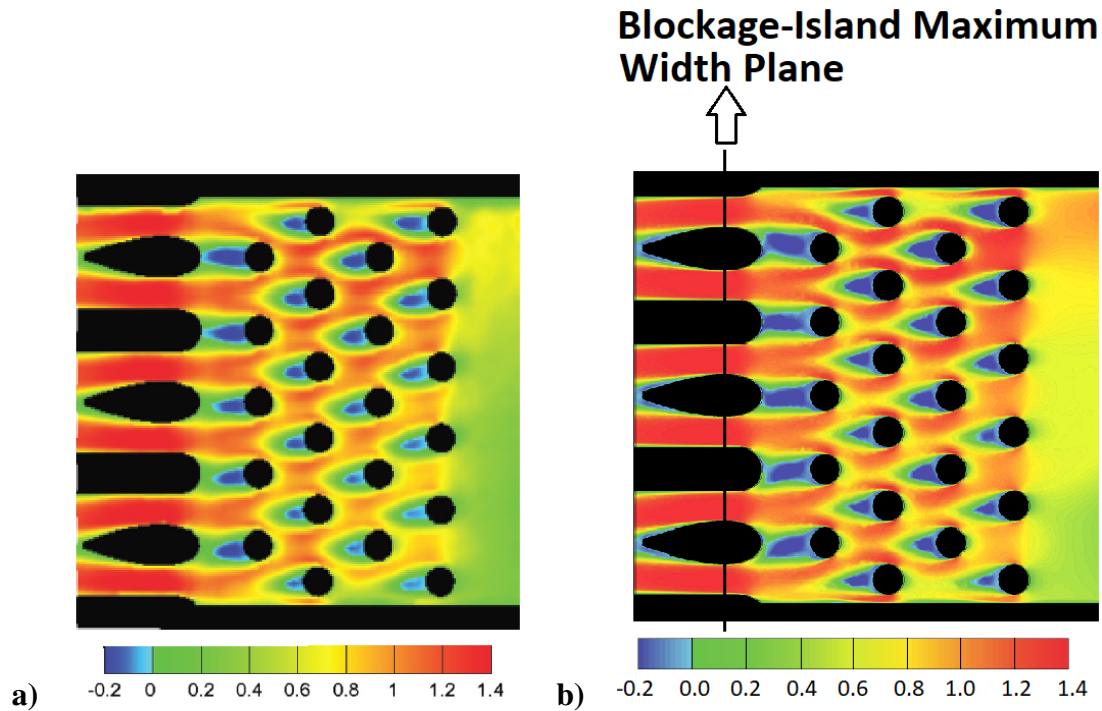


Figure 4.1: Non-Dimensional Streamwise Velocity Contours a) Experimental (Fig. 3 of [3]) , b) Predictions

the plenum section contracts into the constant-height region containing the pin array. According to the orientation of Figure 4.1, the flow enters the domain from the top and from a further upstream location out of the boundaries of the figure, and moves towards left where the slots are located. The effect of this injection is reflected as an increase in the local velocity, both in the contours of the predictions and the data.

The velocity measurement at the location corresponding to the blockage-island maximum width is 0.51 m/s [1]. This value was predicted as 0.52 m/s, resulting in an over-prediction of approximately 2%. In fact, the velocity predictions are found to be in good agreement with the data over the whole domain of Figure 4.1. The separation bubbles are observed to form immediately behind every pin fin within the blue regions in a similar fashion to what the data suggests. These wakes extend towards downstream pins, and the velocity is recovered across the remaining sections of each passage. In the wake of the islands, the flow separation is not as obvious. The data contours show that the flow is redistributed through the pin array; and this is observed in the prediction contours of Figure 4.1 as well. The only significant difference oc-

curs on the right side of the contours that are closer to the manifold entrance where the coolant is introduced into the test section. The assumed velocity profile and turbulence intensity are likely to cause a difference in the predictions at the immediate vicinity of this part of the domain. However, as was mentioned before, the computational studies performed in [1] showed that the coolant inlet conditions did not have a significant impact on the predictions.

4.2 Aerodynamic Results From Comparison Cases

Figure 4.2 shows the streamwise velocity contours at the mid-plane. Similar to the validation case in Figure 4.1 as the flow proceeds through the passage, the regions of reverse flow are formed behind every pin fin. Since the inlet flow is introduced in the streamwise direction and is assumed to be uniform, the flow distribution reflects this inlet condition in the downstream region.

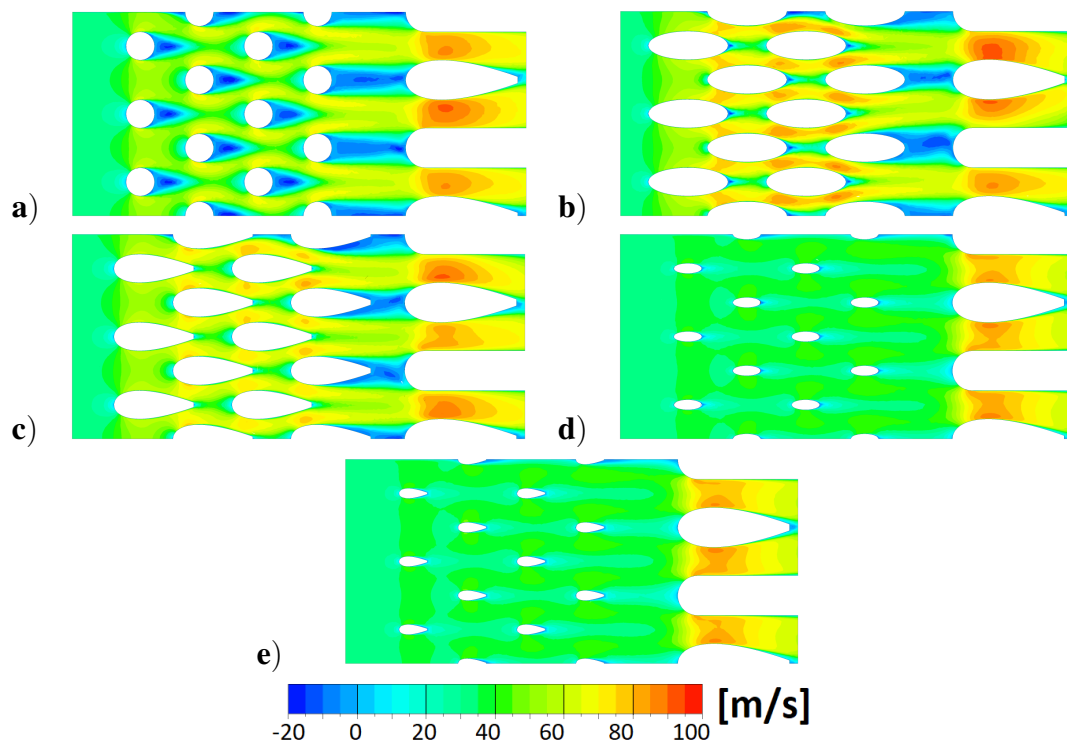


Figure 4.2: Streamwise Velocity Contours a) Circular, b) Elliptical, c) Airfoil Shaped, d) Small-Elliptical, e) Small-Airfoil Shaped

The top side of each contour plot is a physical wall while the bottom side is a symmetry wall. Therefore, the local flow features along these two sides are not necessarily symmetric due to the endwall effects occurring along the top side only. On the other hand, the flow field is symmetric with respect to the symmetry wall, but the other half of the domain is not shown in the figure.

Although the velocity gradients through the circular pin array are mild, they become more significant for the pin shapes of ellipse and airfoil profile. The separation regions are intensified at the last row of pins for these cases. This is mostly due to the relatively short distance between the pin and the blockage surfaces, as well as the lack of another follow-up pin row. While the circular pin rows are totally isolated from each other across the array, elliptical, and airfoil-shaped pin rows are not. Hence, the reduced flow area in between the trailing edge of one row and the leading edge of its downstream row causes an increase in the local velocity.

On the other hand, the wakes of the airfoil-shaped pins across the pin array of case are not obvious, since an airfoil shape will have a reduced separation zone compared to a blunt object such as cylinder or ellipse. For the small elliptical and small airfoil-shaped cases, since the pins are of a smaller size having the same row extents with those of circular case, the interaction between each row is not as significant anymore.

The velocity increases in the flow direction in general, reaching its maximum through the blockage area. Large velocity gradients are observable in this region towards the slot exit both in streamwise and spanwise (along the section width) directions. Due to the overlaps between the rows of cases (b) and (c), the interaction between the pins contribute to the velocity gradients as well. In other words, if the rows are separated from each other, the velocity gradients diminish as is shown in cases (d) and (e). For those cases, a significant velocity gradient is observable only through the blockage area.

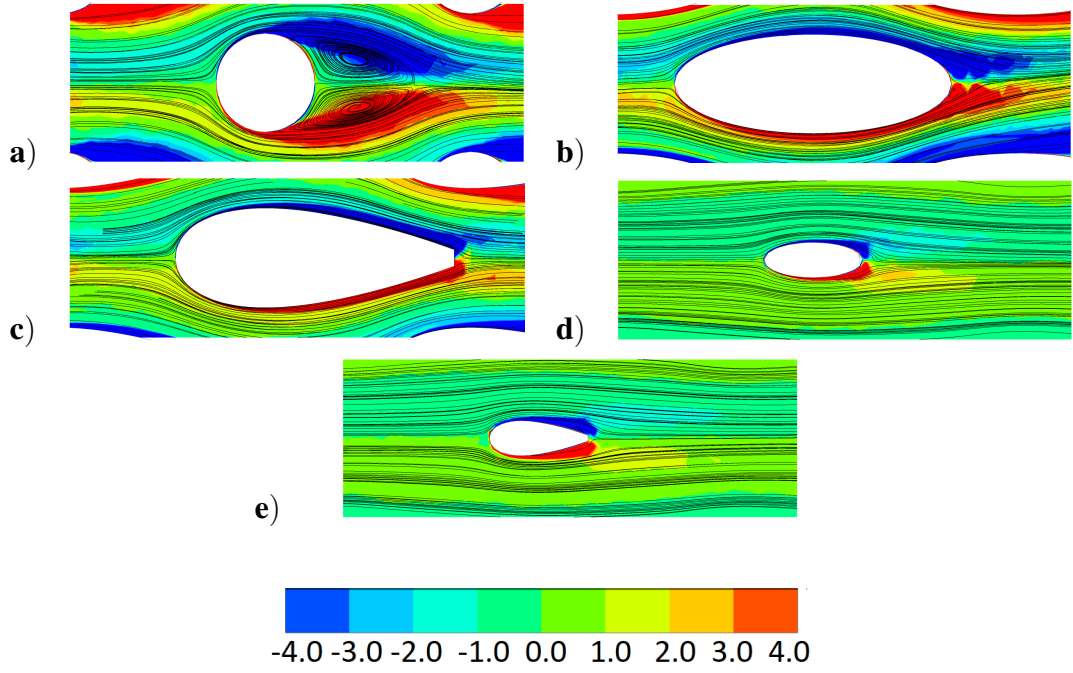


Figure 4.3: Non-Dimensionalized Streamwise Vorticity Contours a) Circular, b) Elliptical, c) Airfoil Shaped, d) Small-Elliptical, e) Small-Airfoil Shaped

In order to have more information on the flow patterns, the streamwise vorticity contours in the mid-plane are examined in Figure 4.3. Vorticity is non-dimensionalized by the air inlet velocity and the section height. The non-dimensionalization method is given by Equation 4.2, where H is the channel height, u_i is the inlet velocity, and the subscript s defines the streamwise direction:

$$\omega_s' = \frac{\omega_s H}{u_i} \quad (4.2)$$

The neighborhood of each pin across an array is dominated by the vortical flow structures. The blunt shape of the circular pin is the one producing the largest wake region where the flow separation occurs. In addition, there are horseshoe vortices occurring along the surfaces of the pins, coinciding with the strong vorticity regions. The wake of the airfoil-shaped pin (c) is significantly smaller than those of (a) and (b), meaning a reduced aerodynamic penalty. With the reduced size of the pins (d) and (e), this penalty is even lower.

Flow features can be examined by looking at the total pressure coefficient, which gives a measure for the total pressure drop in streamwise direction via Equation 4.3:

$$\Psi = \frac{P_T - P_{T,l}}{\rho_i u_i^2 / 2} \quad (4.3)$$

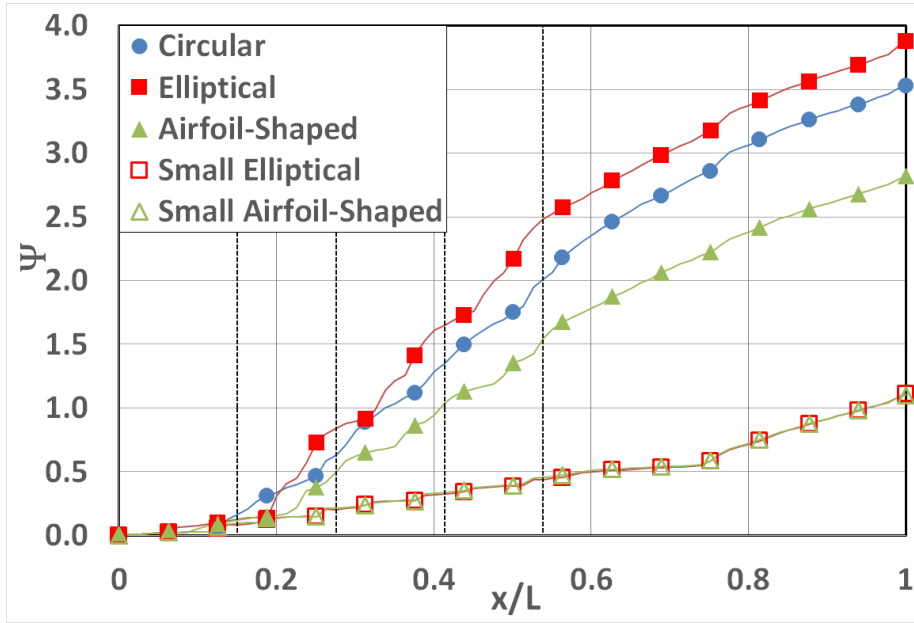


Figure 4.4: Mass Flow-Averaged ψ In Streamwise Direction

In Figure 4.4, this coefficient is mass flow-averaged across the width of the domain, and is shown as a function of the normalized distance from the inlet. To do so, a series of vertical cut planes at different downstream locations were used. Then, the mass flow-average values of Ψ were calculated on these planes. Since there are large velocity variations in the lateral direction, mass flow-averaging was preferred rather than spanwise-averaging to better quantify the parameters of interest, such as loss and entropy generation.

Starting off with the same inlet total pressure, all three configurations cause a consistent increase in Ψ due to the loss accumulation across the domain. In Figure 4.4, the four vertical dashed lines show the locations of the pin centers, which are the same for all five configurations. The configuration with the elliptical pins seems to have the highest amount of loss, followed by the circular pins and the airfoil-shaped

pins. Although this seems contrary to the findings of [14] regarding the performance of elliptical and circular pins, the elliptical pins in this study have significantly larger wetted areas resulting in higher viscous dissipation and hence higher losses. However, even if the airfoil-shaped pin has also a large wetted area, the lessened aerodynamic penalty for this shape is remarkable. For the small size elliptical and airfoil-shaped pins, the aerodynamic penalty is significantly less due to the shrinkage in the surface area.

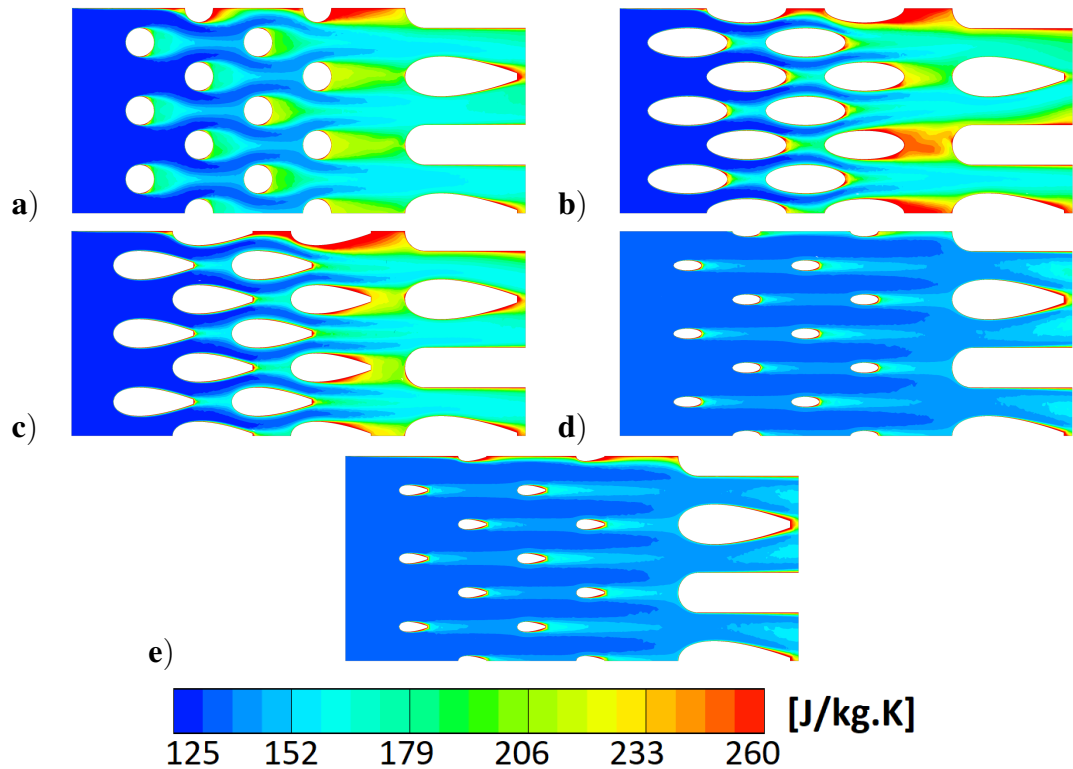


Figure 4.5: Entropy Contours a) Circular, b) Elliptical, c) Airfoil Shaped, d) Small-Elliptical, e) Small-Airfoil Shaped

More insight into the loss mechanism can be gained if the entropy generation across the domain is analyzed. Figure 4.5 demonstrates the top view of the section mid-plane with the entropy contours. The general trends show a consistent entropy generation in the streamwise direction for all five configurations. The top side of the domain is a solid wall while the bottom side is a symmetry wall. Substantial losses in the domain occur by the walls due to the effects of viscosity, which is indicated by the red color. When the flow reaches the trailing edges of the airfoil-shaped pin and blockage

surfaces, losses add up due to the local acceleration and mixing of the surface flows. This is more significant at the blockage trailing edges. The entropy generation is the largest for the elliptical pins, followed by the circular and airfoil-shaped pins, due to the large wake regions behind the pins. It is hard to distinguish the contours of the small elliptical and small airfoil-shaped pins. Hence, their loss characteristics are very similar.

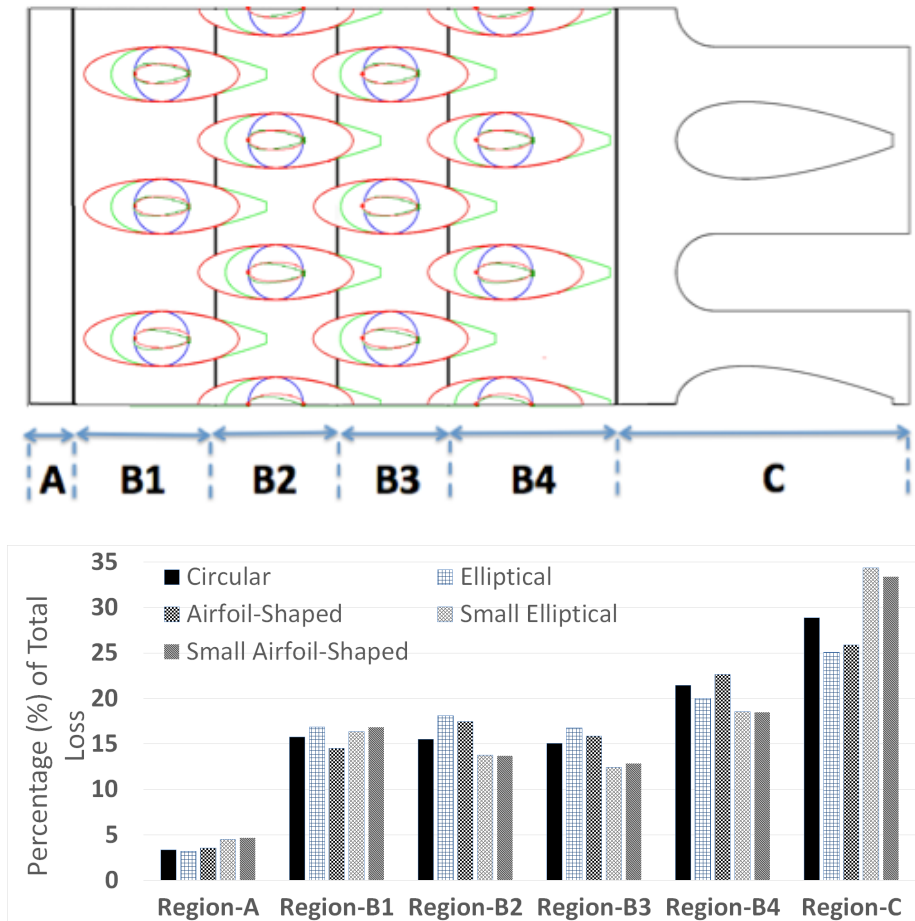


Figure 4.6: Loss Split Per Region

In order to quantify the loss amount for each configuration in more detail, the computational domain is split into six regions, as in Figure 4.6. Region A represents the inlet section, Region B is the pin array, and Region C consists of the remaining portion with the lands and the blockages. The layout given here shows the five configurations superimposed on top of each other. The split planes are located approximately a one-pin diameter (1D) away from the row centerlines. The first and last planes are further

away from the nearby centerlines, approximately 1.5D and 2D, respectively, in order to include the extensions of the larger pin shapes. Region B is further split into row-by-row sections. Due to the dimensions of the shapes, the circular pins remain between the planes, while the leading edge of the large elliptical pins and the trailing edge of the large airfoil-shaped pins run over the planes. However, with this approach the loss quantification can be simplified reasonably.

For the loss audit, the mass flow-averaged entropy value for each cutting plane (s_l , l for local) was compared with the mass flow-averaged entropy value of the previous plane (s_{up} , up for upstream), according to Equation 4.4:

$$TotalLoss\% = \frac{s_l - s_{up}}{s_e - s_i} \times 100 \quad (4.4)$$

where the difference is normalized by the total increase between the inlet and exit planes of the domain.

The loss amount does not accumulate much in Region A, as this is the shortest region and there are no cross-pin effects due to the absence of the pin structures. As the flow starts going through the pin array, a significant rise occurs in the loss for all configurations, and the loss stays at similar levels across the pin rows. All pins experience elevated levels of entropy generation in Region B4. This region is where the wakes of pins are strongly experienced due to a combined effect of the absence of another downstream row of pins and the interaction with downstream lands and blockages that are located in close proximity. Finally, the largest amount of losses for all five configurations occurs in Region C.

Figure 4.6 provides information on the loss split across the domain for each configuration, but it does not compare the loss amounts between configurations. For this, the maximum mass flow-averaged entropy on the exit split plane across all five configurations is used to normalize the local mass flow-averaged entropy on the planes splitting the domain. This is defined as the entropy ratio on the y-axis of Figure 4.7, and its variation is given as a function of x/L . The vertical dashed lines are attached to the plot to identify the pin locations.

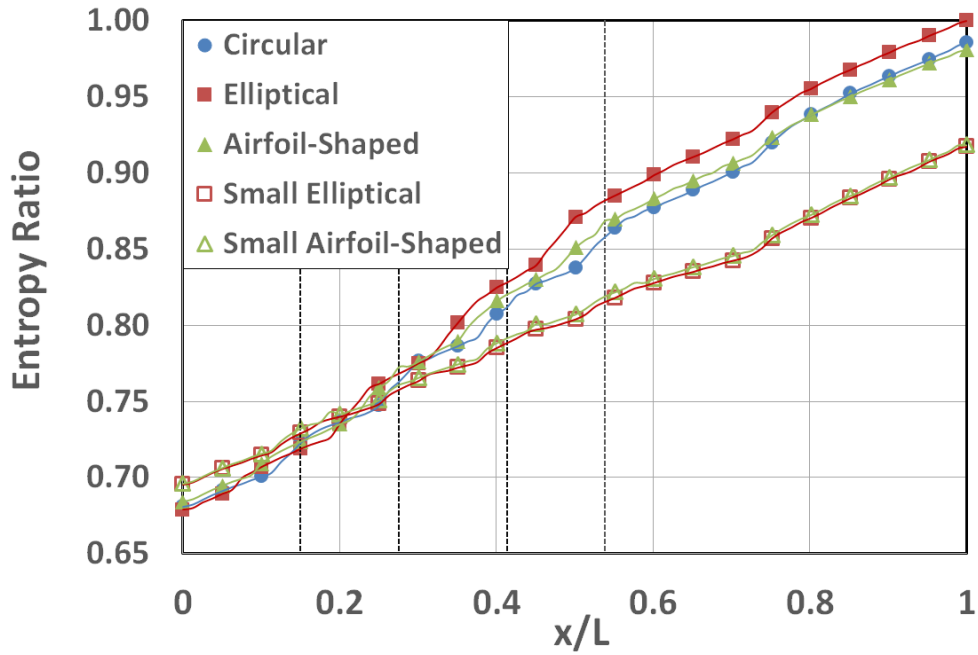


Figure 4.7: Mass Flow-Averaged Entropy In Streamwise Direction

Figure 4.7 presents the mass flow-averaged entropy values, with similar trends to Ψ variation of Figure 4.4. Comparing the general trends in these figures, it is clear that the overall loss generation is greater for the elliptical pins, leading the circular and airfoil-shaped pins by a small difference of around 2%. The small pins generate less penalty. It can be concluded from this discussion that losses could be reduced if the downstream slot section was kept further apart from the last row of pins for the given pin dimensions relative to the domain. Since the rows were not totally isolated for the elliptical and airfoil-shaped pins, the interaction between the rows also contributes to the overall loss mechanism. The losses are further reduced if the pins are of smaller size. The difference between the two small pins is almost negligible, and their curves are almost identical. They provide aerodynamics savings of approximately 7-8% compared to their larger size partners.

4.3 Thermal Results From Comparison Cases

The convection heat transfer coefficient, HTC, was evaluated on the upper wall of the domain. For the calculations, the bulk fluid temperature, T_{bulk} , the wall temperature,

T_{wall} , and the wall heat flux, q'' , were used as shown in Equation 4.5:

$$q'' = HTC \times (T_{wall} - T_{bulk}) \quad (4.5)$$

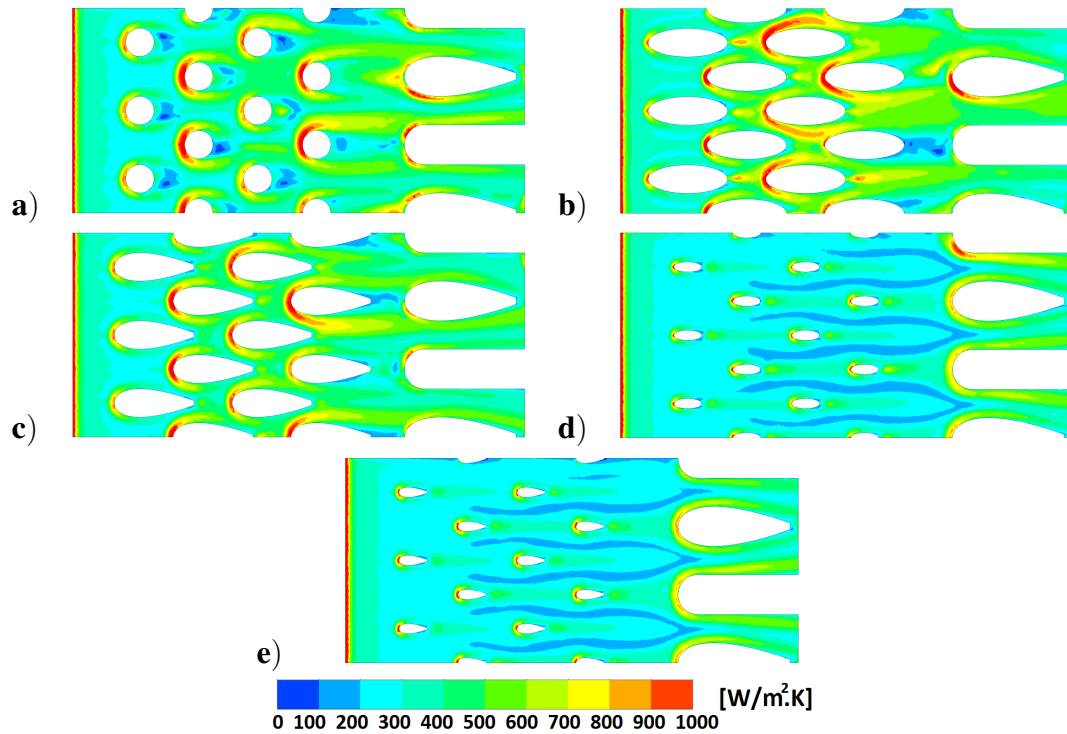


Figure 4.8: Heat Transfer Coefficient Contours a) Circular, b) Elliptical, c) Airfoil Shaped, d) Small-Elliptical, e) Small-Airfoil Shaped

The bulk temperature was calculated as the mass flow-averaged temperature on the spanwise planes in order to take into account the streamwise temperature of the coolant. The HTC contours give the highest levels at the stagnation locations on the pin surfaces as well as on the downstream blockage frontal areas. The horseshoe vortices rolling up around the pin surfaces coincide with the traces of high heat-transfer regions. The levels are reduced significantly for the smaller size pins, hinting that the heat transfer performance of these pins will not be as good.

Additionally, Nusselt number was calculated using Equation 4.6:

$$Nu = \frac{HTC \times D}{k_f} \tag{4.6}$$

where D is the pin diameter, and k_f is the thermal conductivity of air as the working fluid that has a value of 0.0261 W/m.K . The Nusselt number calculations are compared to the data set provided by Metzger et al. [4]. This data is presented in Figure 4.9.

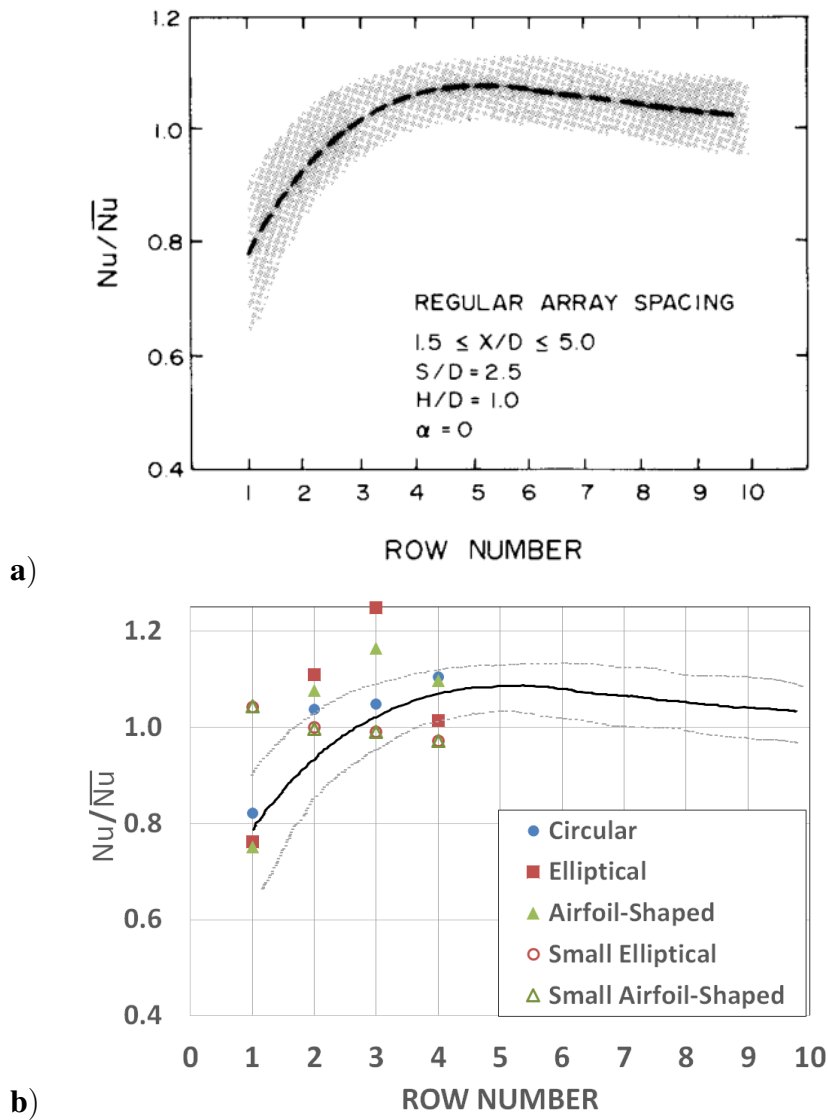


Figure 4.9: Normalized Nusselt Numbers For Pin Arrays a) Experiment (Fig. 4 of [4]), b) Predictions

In this study, Metzger et al. [4] defines a row-averaged Nusselt number (Nu) and an array-averaged Nusselt number (\bar{Nu}). The shaded band consists of the data from circular pins with Reynolds number ranging from 2310 to 51740. Figure 4.9 shows the prediction results with respect to this band. The pin-array structures had $X_p/D = 2.4$, $S_p/D = 2.4$, and $H_p/D = 1$. Here, X_p is the lateral distance between the pins, S_p is the streamwise distance between the pins, and H_p is the pin height. The flow Reynolds number was calculated to be 52375. Considering that these values are within close range of the data of Figure 4.9, a comparison can be performed with the predictions of this study. The prediction results reasonably fell into or around the shaded band. Considering that the data represents the circular pins, the observable mismatch of the predictions for the elliptical and airfoil-shaped pins is understandable.

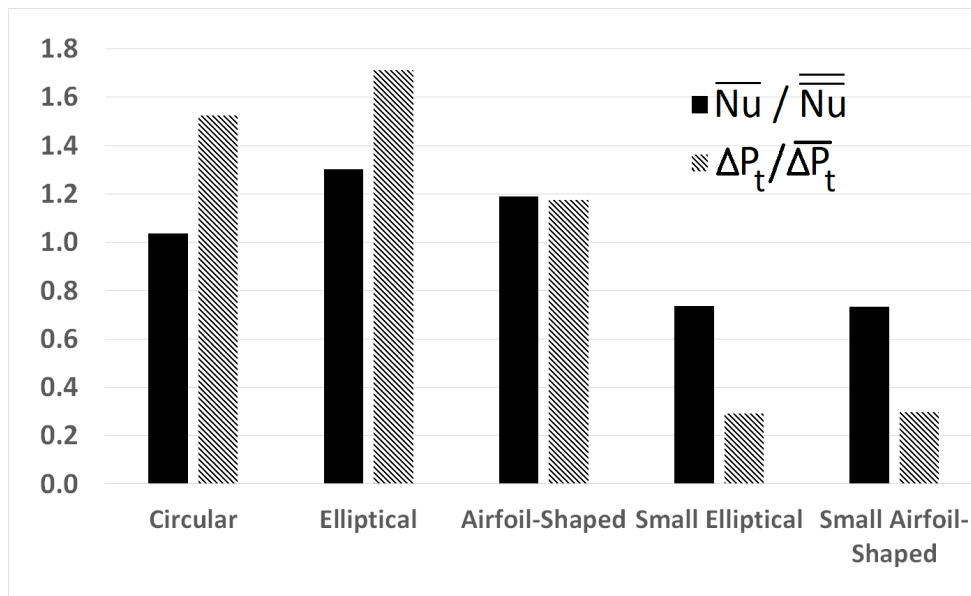


Figure 4.10: Loss And Thermal Comparison Of Pin Arrays

Figure 4.10 summarizes the findings of the internal comparison study. The bars filled with diagonal stripes presented in the figure represents the ratio of total pressure loss along section B to the average total pressure loss of all five pin arrays. The black bars represent the ratios of the array averages to the overall average of all five pin arrays for Nusselt number. According to this comparison, the airfoil-shaped pins bring aerodynamics savings due to their significantly-reduced wake region, compared to the pins of similar size. For the two small-size pins, the differences between the aero-

dynamics and thermal characteristics are not distinguishable. Although the pressure loss is significantly reduced, the heat transfer performance is reduced as well.

CHAPTER 5

EXTERNAL COOLING ANALYSIS & RESULTS

In this chapter, the analysis and results of the external cooling study are presented. First, the validation of model is presented and the results for the validation study are discussed. Later, the details of the comparison study are explained. Here, the comparison study results are again demonstrated both from an aerodynamics and a thermal perspective. The results obtained from five different pin-fin geometries are compared.

5.1 Validation

The comparison between the predictions and the experiment is shown in Figure 5.1 in the form of contours of non-dimensional streamwise velocity component through the pin arrays and the slot exit of the test configuration. The non-dimensionalization method is given by Equation 4.1 where u_s is the local coolant velocity. The details of the validation of the internal cooling case was explained in Section 4.1. Here, the validation of the flow field downstream of the slot exit is performed and the predictions are compared with the experiments of Ling et al. [3].

According to the orientation of Figure 5.1, the coolant enters the domain from the left side where the slot exit is located and then it mixes with the main flow. The shown section is the plane 2 mm above the breakout surface and provides a top view of the downstream flow field. The black region represents the solid land. The top and bottom sides are the symmetry walls. The use of the symmetry walls has enabled to cut down the computation time significantly. From Figure 5.1 it can be seen that the low-momentum wake behind the airfoil-shaped blockages and pin fins extend far

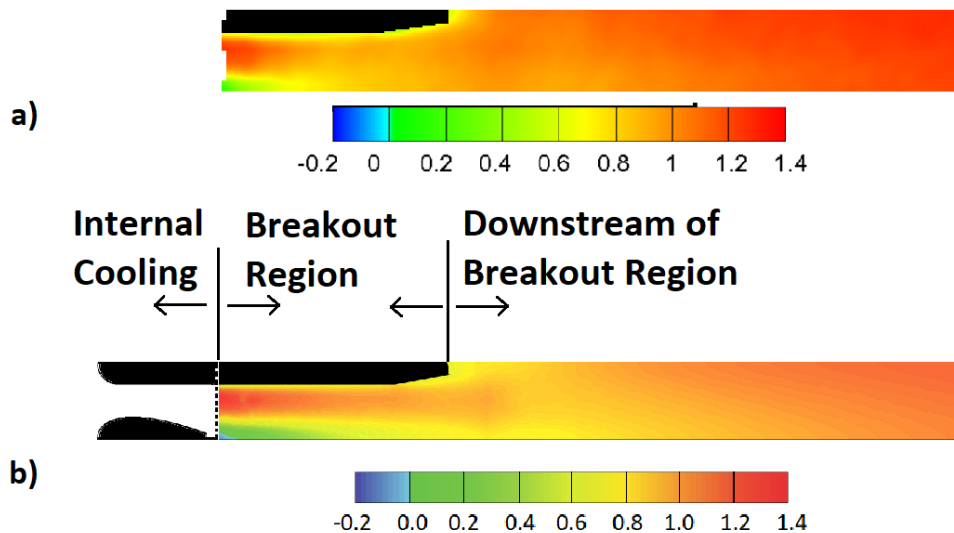


Figure 5.1: Non-Dimensional Streamwise Velocity Contours Downstream Of Slot Exit a) Experimental (Fig. 3 of [3]) , b) Predictions

downstream in the contours for the predictions. This under-prediction behavior with $k - \omega$ SST turbulence model is reasoned with the insufficient turbulent viscosity [1]. Although the mixing process of the coolant with the mainstream flow seems to occur slower in the predictions compared to the experiment, the velocity predictions are generally found to be in good agreement with the data over the whole domain.

5.2 Aerodynamic Results From Comparison Cases

Figure 5.2 shows the streamwise velocity contours at the mid-plane above the breakout surface for all five configurations. Reverse flow regions due to mixing are seen at the land tip and locally at the breakout region. Further downstream of the slots, the velocity increases in the flow direction. Flow patterns for all cases are the same downstream of the breakout region but shows minor differences at the breakout right at the slot exit.

To see the development of the flow on the breakout surface, a more detailed analysis is pursued. Planes perpendicular to the streamwise direction are created at every 5 mm (1H) distance starting from the slot exit, where H is the slot exit height. Vorticity contours with velocity fields are presented in Figures 5.3, 5.4, 5.5, 5.6, 5.7. The left

sides of the figures are symmetry walls, while the right sides are solid land walls. Vorticity is non-dimensionalized by the air inlet velocity and the section height as described in Section 4.2.

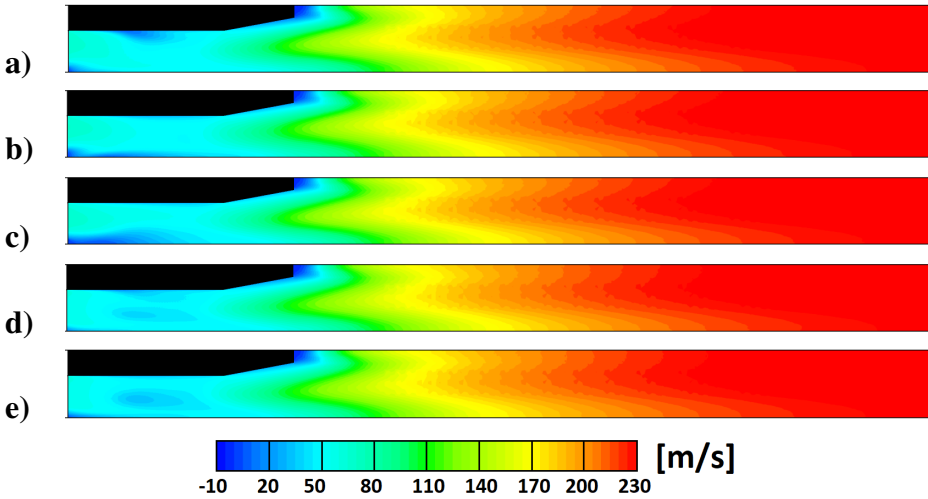


Figure 5.2: Streamwise Velocity Contours Downstream Of Slot Exit a) Circular, b) Elliptical, c) Airfoil Shaped, d) Small-Elliptical, e) Small-Airfoil Shaped

Figure 5.3 shows the non-dimensional streamwise vorticity contours at the slot exit. Regions represented by contour colors smaller than zero indicate clockwise rotation (blue color) while contour colors greater than zero indicate counterclockwise rotation (red color). Circular and elliptical cases show similar vortical structures while the airfoil-shaped case generates reversed vortices near the symmetry wall. A change in the size decreases the strength of this structure in both airfoil-shaped and elliptical pin cases. The large vortical structures observed become smaller for the small size pins. The reason for that is the longer distance between the slot opening and the last row of small pins than the first three cases. The weaker vortices behind the small pins find enough room to diminish in the flow direction. It can be said that for small pins, the flow structure at the slot is mostly generated by the airfoil-shaped blockage just before the slot exit.

The similarity between the circular and elliptical, and the small elliptical and small airfoil-shaped cases is obvious in the velocity boundary conditions given in Figure 3.15 as well. In Figure 5.3, for all cases, the velocity vectors are directed to the sym-

metry wall. This is expected since the domain is continuous here and the flow moves in this direction due to the existence of the airfoil-shaped blockages right upstream of the slot exit in the internal cooling channel.

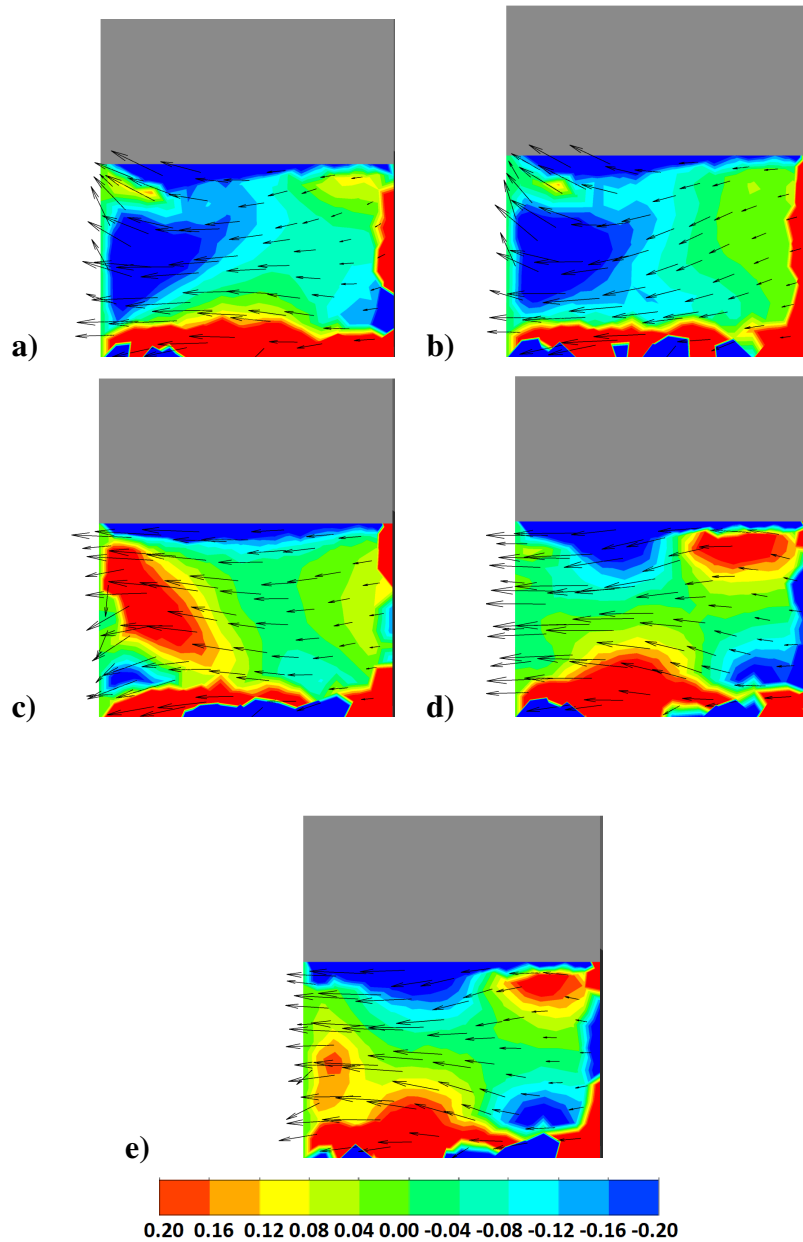


Figure 5.3: Streamwise Non-Dimensional Vorticity Contours With Velocity Vectors At Slot Exit a) Circular, b) Elliptical, c) Airfoil Shaped, d) Small-Elliptical, e) Small-Airfoil Shaped

Figure 5.4 shows the non-dimensional streamwise vorticity contours at 1H down-

stream of the slot exit. For all cases, the velocity vectors have changed their directions, and the flow moves upward instead of traveling towards the symmetry wall.

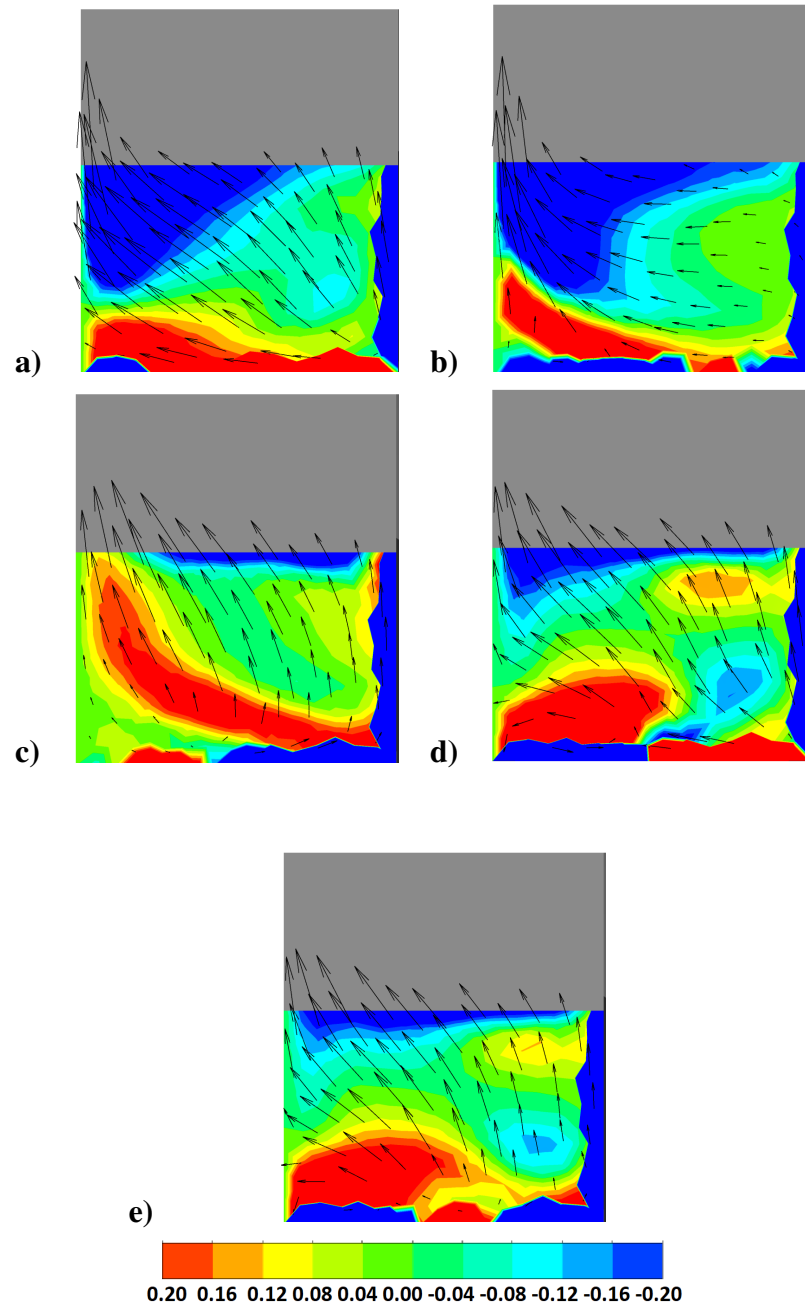


Figure 5.4: Streamwise Non-Dimensional Vorticity Contours With Velocity Vectors At 1H Downstream Of Slot Exit a) Circular, b) Elliptical, c) Airfoil Shaped, d) Small-Elliptical, e) Small-Airfoil Shaped

This is due to the interaction between the main flow and the coolant blown out from

the slot exit. At this plane, due to the mixing of the main flow with the coolant, the strength of both clockwise and counterclockwise vortices have increased. The similarity between the circular and elliptical cases as well as the small pins still exist in this plane.

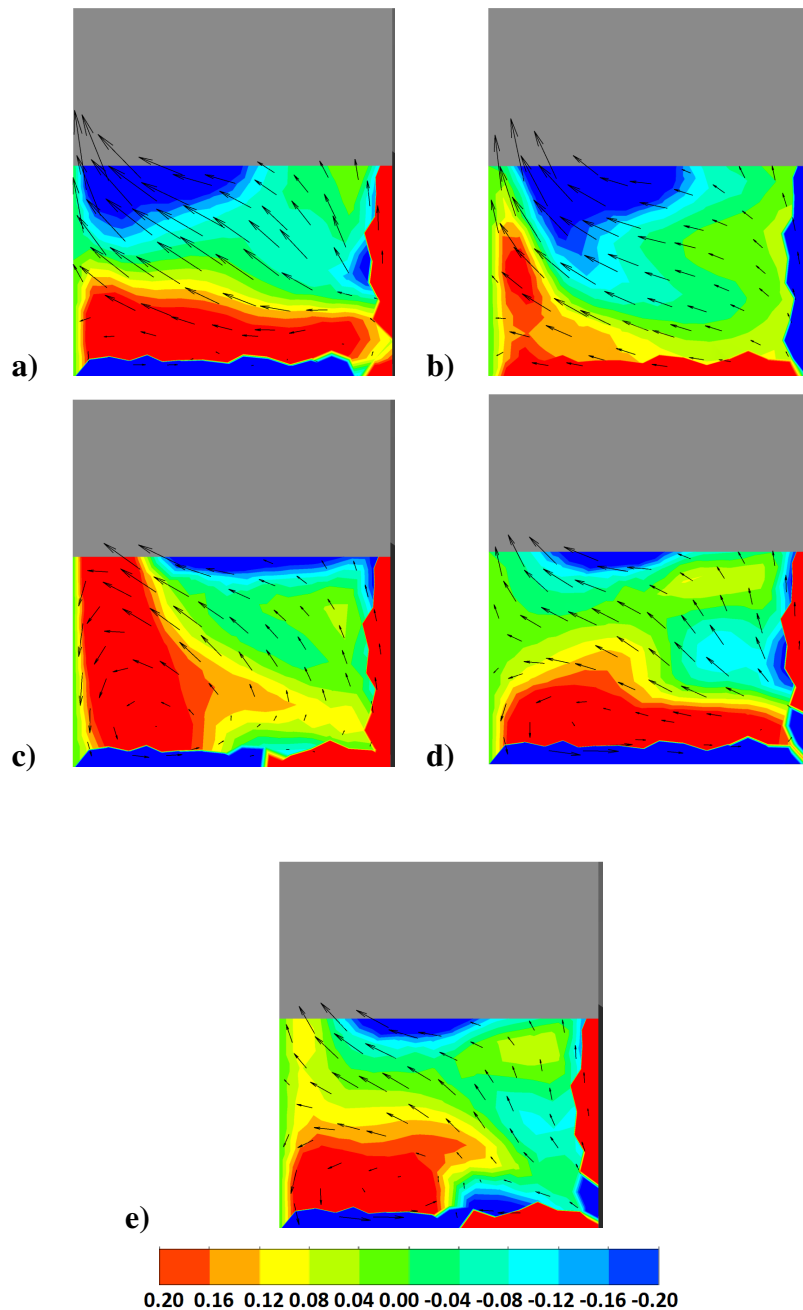


Figure 5.5: Streamwise Non-Dimensional Vorticity Contours With Velocity Vectors At 2H Downstream Of Slot Exit a) Circular, b) Elliptical, c) Airfoil Shaped, d) Small-Elliptical, e) Small-Airfoil Shaped

Figure 5.5 shows the non-dimensional streamwise vorticity contours at $2H$ downstream of the slot exit. In this plane, it is observed that the strength of clockwise vortices (blue regions) have decreased, while the counterclockwise vortices have gained strength. Considering the direction of the velocity vectors, it can be said that the mixing process still continues.

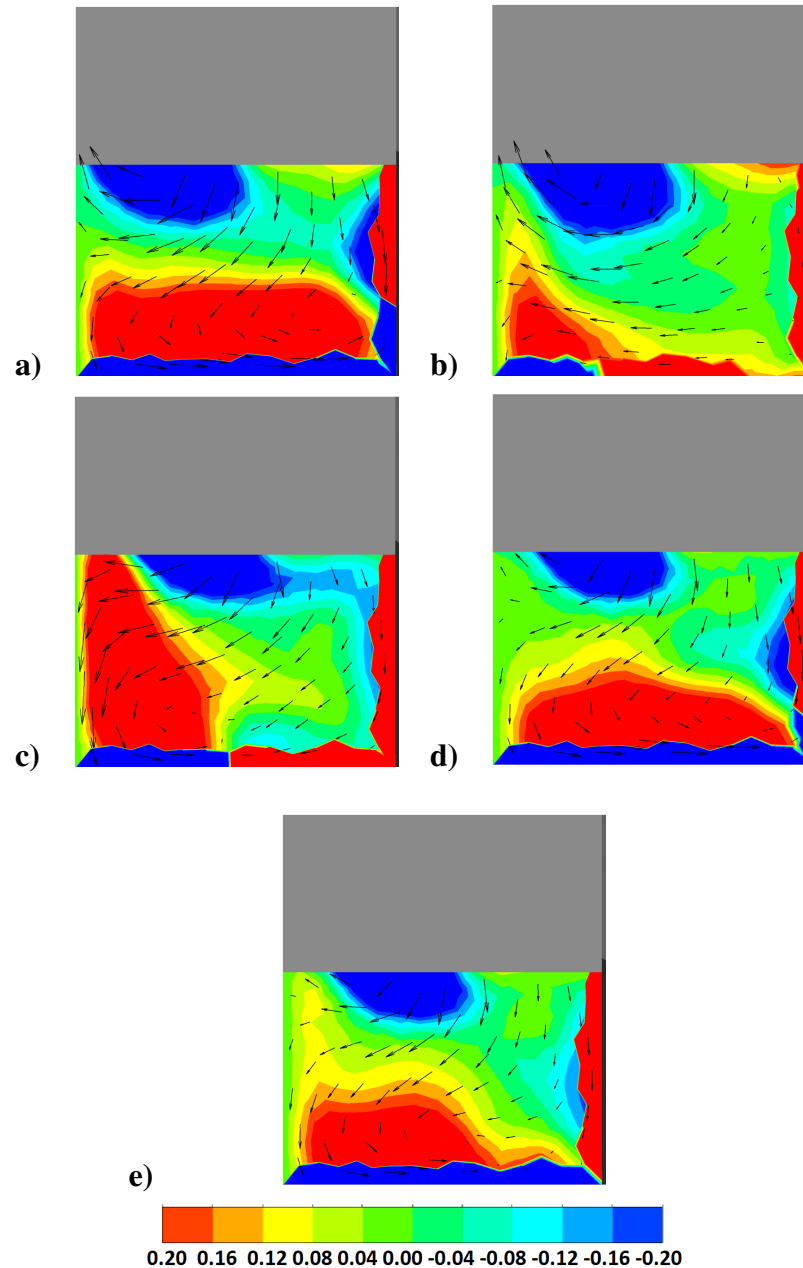


Figure 5.6: Streamwise Non-Dimensional Vorticity Contours With Velocity Vectors At $3H$ Downstream Of Slot Exit a) Circular, b) Elliptical, c) Airfoil Shaped, d) Small-Elliptical, e) Small-Airfoil Shaped

Figure 5.6 shows the non-dimensional streamwise vorticity contours at 3H downstream of the slot exit. Starting from this plane, the change in the vorticity contours becomes less obvious. For all cases, a notable difference between 5.5 and Figure 5.6 is the change in the direction of the flow in the plane. Other than that, the velocity

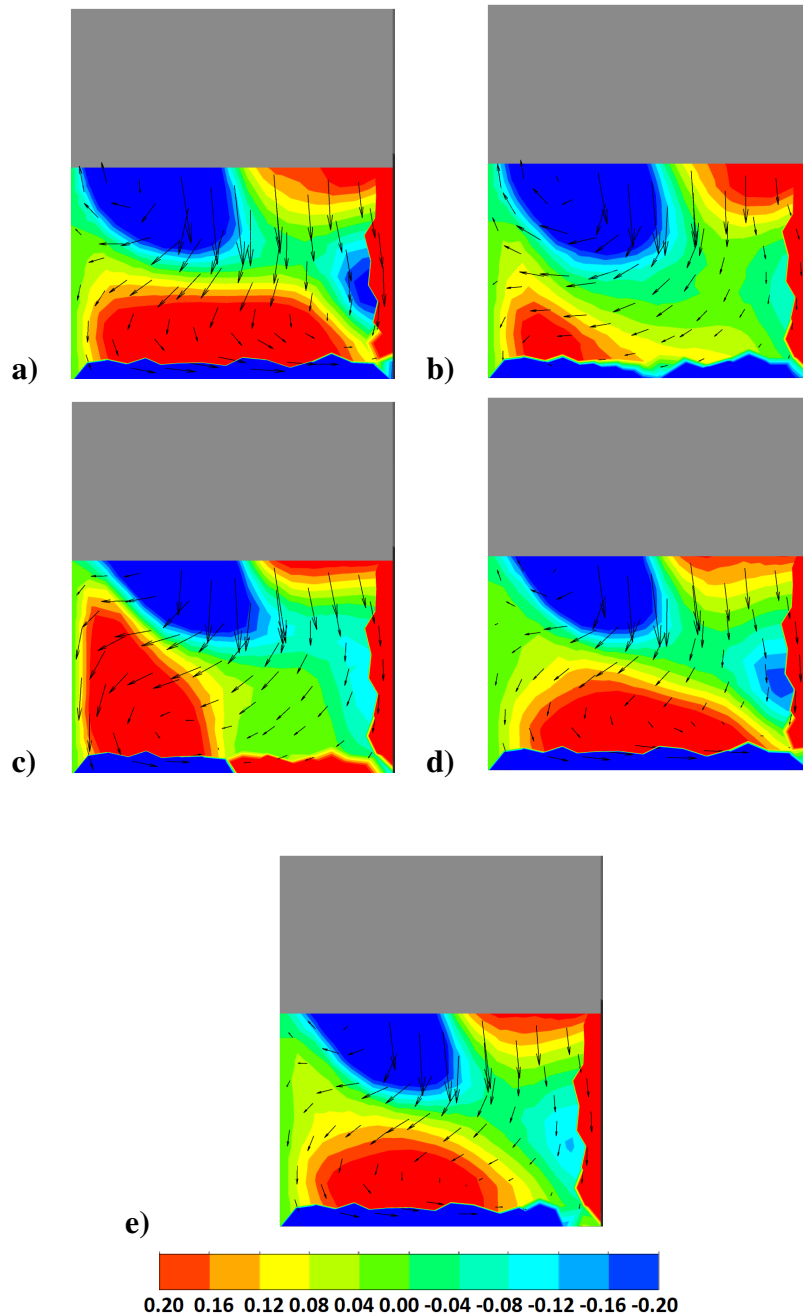


Figure 5.7: Streamwise Non-Dimensional Vorticity Contours With Velocity Vectors At 4H Downstream Of Slot Exit a) Circular, b) Elliptical, c) Airfoil Shaped, d) Small-Elliptical, e) Small-Airfoil Shaped

vectors and the vorticity contours look similar. This indicates that the effect of the inlet conditions applied at the slot opening has spanned a distance of $3H$ downstream of the slot exit, and beyond that the main flow conditions suppress the impact of the coolant flow and dominate the flow region.

Figure 5.7 proves that the effect of coolant has disappeared. There are small differences in the velocity field and the vorticity contours between $3H$ and $4H$ downstream of the slot exit. The differences are generally seen near the wall sides, which seem to be the effect of the boundary layer.

The development of the flow field at the breakout surface is summarized in 5.8. For all five cases, the vorticity contours at the first 25 mm distance from the slot opening are presented with 5 mm intervals. The first five of six planes are explained in Figures 5.3, 5.4, 5.5, 5.6, 5.7. The last plane is generated to show that the flow field becomes stable. By looking at the big picture presented in Figure 5.8, the pin shape effect is dominant till $3H$ downstream of the slot, but further downstream, the main flow conditions for all cases are the same and the mixed coolant does not reflect the effects of the pin shapes anymore.

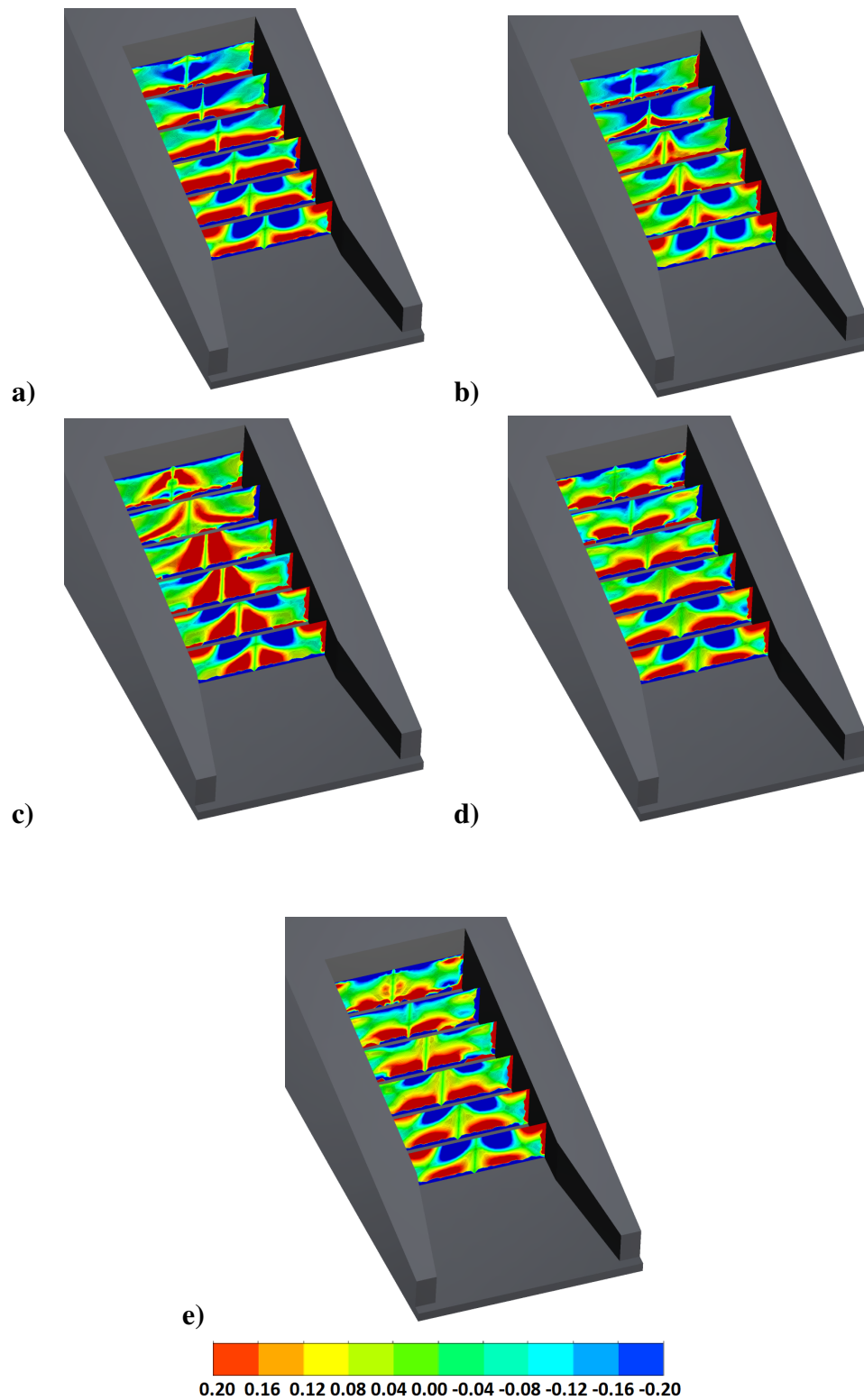


Figure 5.8: Streamwise Non-Dimensional Vorticity Contours Downstream Of Slot Exit a) Circular, b) Elliptical, c) Airfoil Shaped, d) Small-Elliptical, e) Small-Airfoil Shaped

5.3 Thermal Results From Comparison Cases

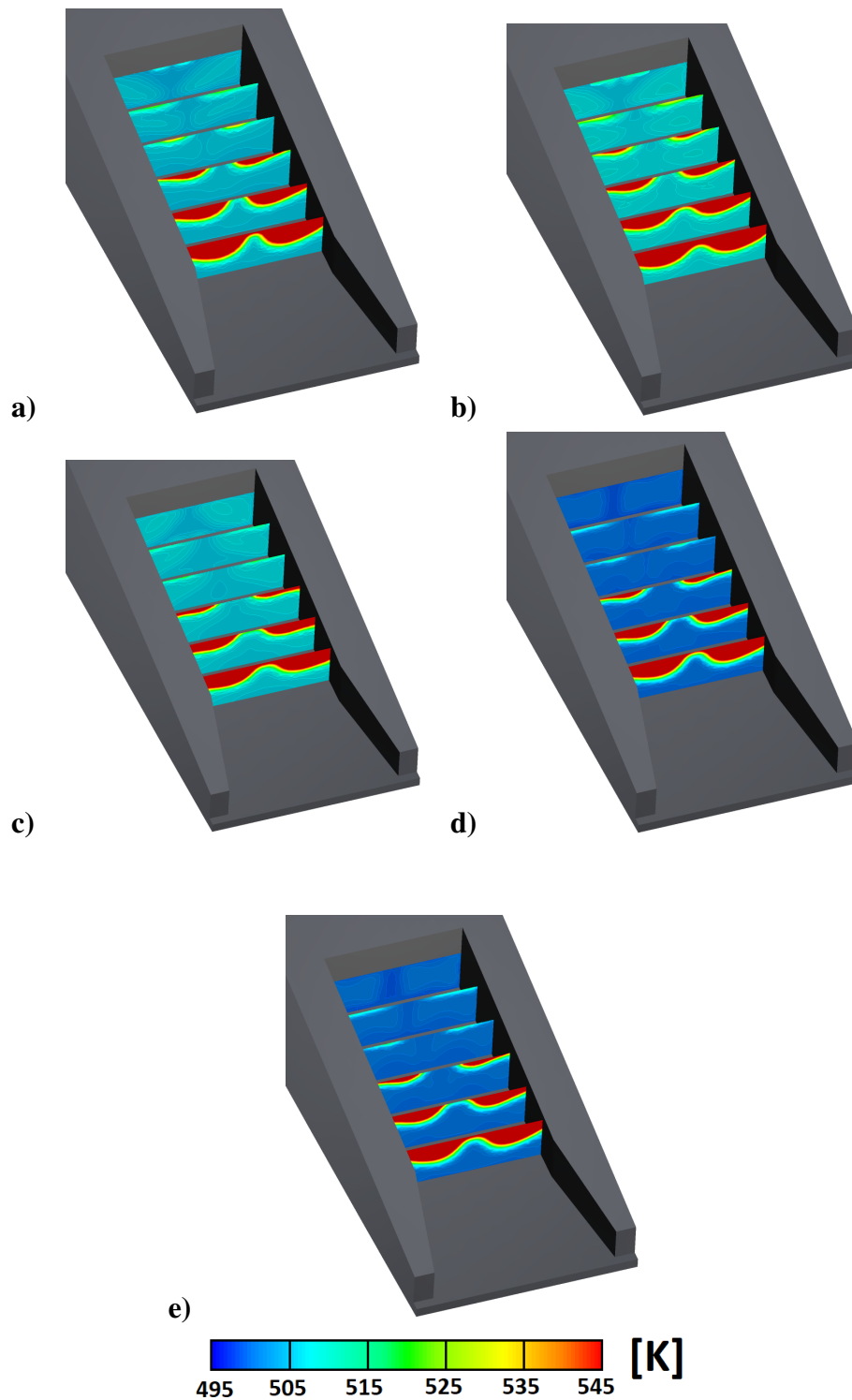


Figure 5.9: Total Temperature Contours Downstream Of Slot Exit a) Circular, b) Elliptical, c) Airfoil Shaped, d) Small-Elliptical, e) Small-Airfoil Shaped

Figure 5.9 presents the total temperature contours on some cross-sectional planes at the downstream of the slot exit along the streamwise direction. For all five cases, the total temperature contours at the first 25 mm distance from the slot opening are presented with 5 mm intervals. At the slot exit, coolant temperature levels are low and they increase in the flow direction. This is because as soon as the coolant exits the slot, it starts mixing with the surrounding hot mainstream. These thermal mixing patterns of the coolant and the main stream flow show similarities for all cases. Total temperature levels are much lower for the small-sized cases since the coolant temperatures are lower.

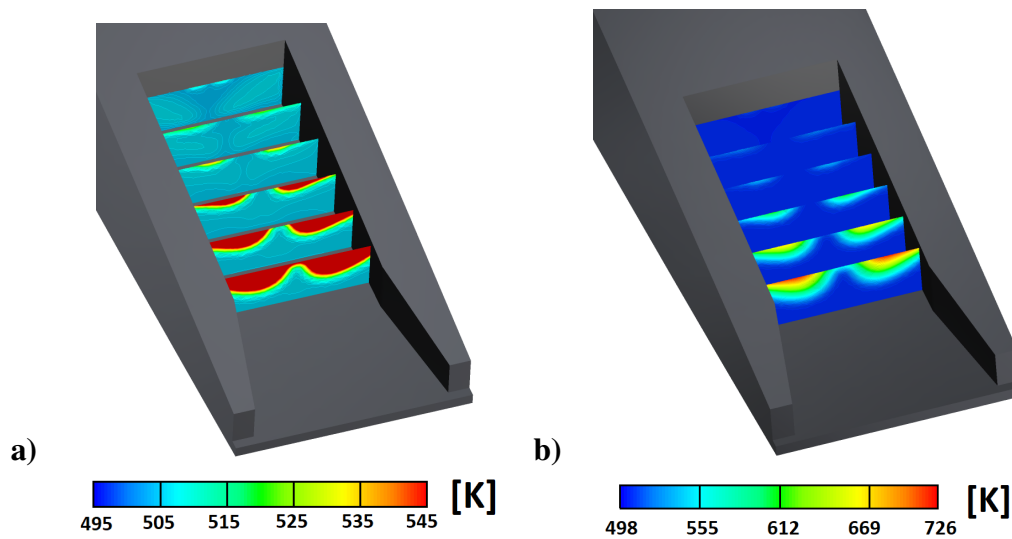


Figure 5.10: Total Temperature Contours With Different Temperature Ranges for Case (a)

The differences between the cases over the whole breakout region are distinguishable with the temperature range used in Figure 5.9. On the other hand, the temperature distribution on the cut planes can be resolved better if a temperature range that includes the highest temperature value is used. On the last plane, the temperature reaches up to 726 K. Temperature gradients due to mixing of the coolant and the mainstream flow can be seen especially on the last plane of Figure 5.10 part (b).

The performance of film cooling can be demonstrated with the use of film-cooling effectiveness. It is calculated with Equation 5.1 where $T_{s\infty}$ is the main flow static temperature of 777.5 K, T_{wall} is the wall temperature calculated by the CFD anal-

ysis, and T_c is the coolant temperature calculated as the mass flow averaged static temperature at the slot exit that was obtained from the calculations of internal cooling.

$$\eta = \frac{T_{s\infty} - T_{wall}}{T_{s\infty} - T_c} \quad (5.1)$$

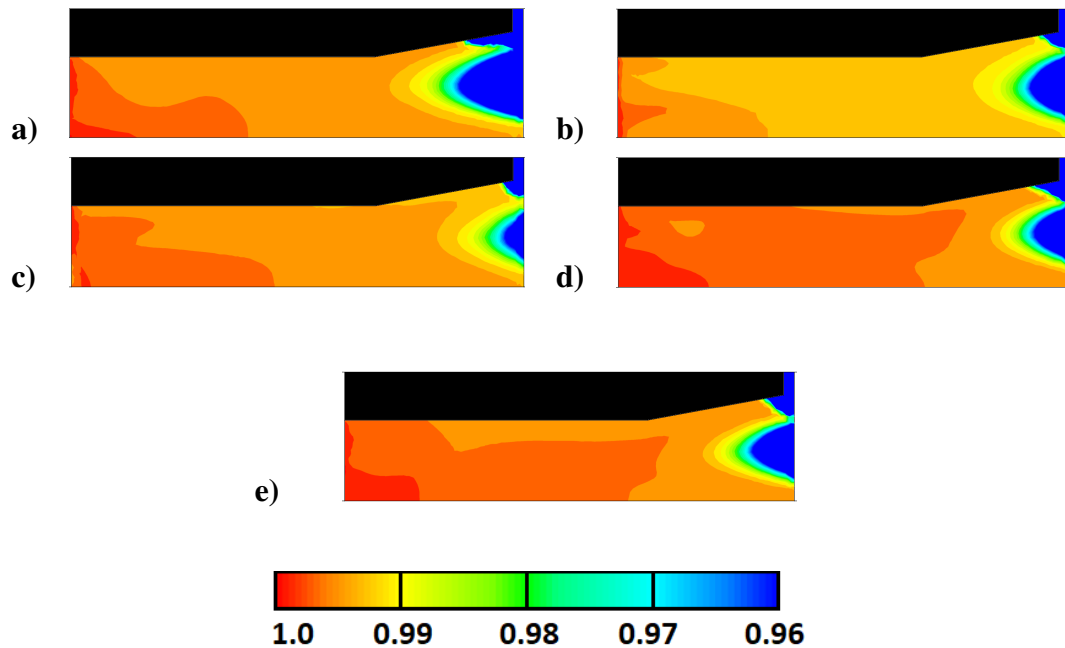


Figure 5.11: Film Cooling Effectiveness Contours At Breakout Surface a) Circular, b) Elliptical, c) Airfoil Shaped, d) Small-Elliptical, e) Small-Airfoil Shaped

In order to display the effects of different pin shapes, the film-cooling effectiveness contours for all five cases are presented at the breakout surface in Figure 5.11. At the slot exit, the effectiveness levels are high and they diminish in the flow direction. For the small elliptical and small airfoil-shaped pins, the effectiveness shows a relatively slow decrease and a similar behavior regarding the film-cooling performance of these pins. This is related to the internal cooling performance of the small pins. Due to their lower heat transfer performance in the internal channel, the coolant temperature did not increase too much. Hence, the heat capacity of the coolant results in higher film effectiveness for external cooling. Similarly, the coolant temperature at the slot exit for the circular pin case is a little bit less than that of the elliptical and

the airfoil-shaped cases, which increased the film cooling capacity. Since the coolant temperature for the elliptical case is the highest one among all cases, film-cooling effectiveness levels for this pin shape are found to be the lowest.

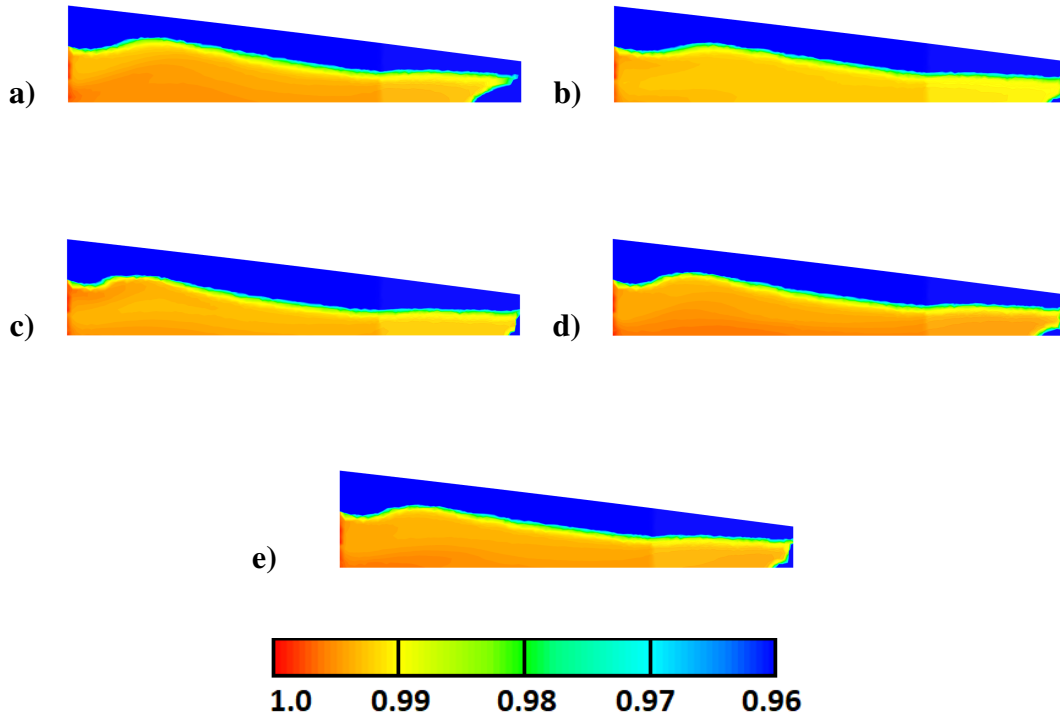


Figure 5.12: Film Cooling Effectiveness Contours at Land Side Wall a) Circular, b) Elliptical, c) Airfoil Shaped, d) Small-Elliptical, e) Small-Airfoil Shaped

As the coolant passes between the two lands, it cools not only the breakout surface but also the side walls of the lands. Therefore, studying the film-cooling effectiveness also on the land side wall will give important clues about the performances of different pin shapes. Figure 5.12 shows the film-cooling effectiveness contours on the side wall of a land. The coolant is ejected over the breakout surface right at the slot exit, while the mainstream flow partially fills this section that is split with the slot lip located above the slot exit. The effect of this mainstream flow is shown with the blue region. The thermal patterns of the coolant flow and the mainstream mixing are similar for all cases. As in the breakout surface film-cooling effectiveness, the land side film-cooling effectiveness levels are directly related to the slot exit temperatures of the coolant.

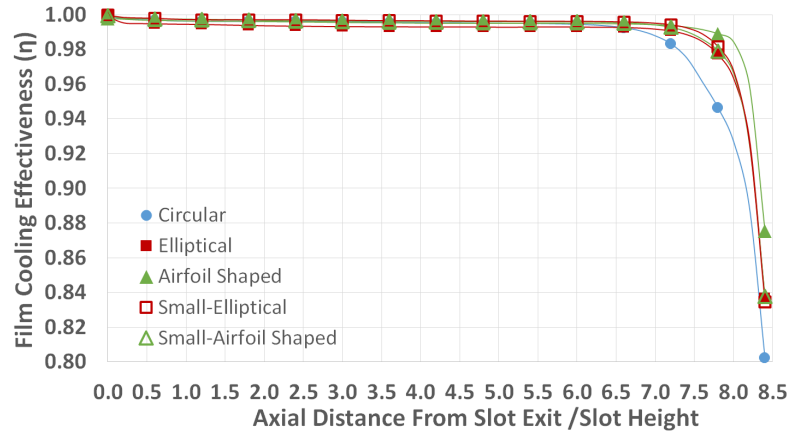


Figure 5.13: Laterally-Averaged Film Cooling Effectiveness at Breakout Surface

The contour plots of film-cooling effectiveness reveal how the effectiveness diminishes at the breakout surface. To compare overall film-cooling performances of different pin shapes, the film-cooling effectiveness along the breakout surface is averaged in the lateral direction. Figure 5.13 shows the laterally-averaged film cooling effectiveness at the breakout surface. The vertical axis shows the laterally-averaged film-cooling effectiveness, while the horizontal axis shows the ratio of the axial distance from the slot exit (X) to the slot height (H). $X/H=0$ is the slot exit, and $X/H=8.4$ is the exit of the breakout surface.

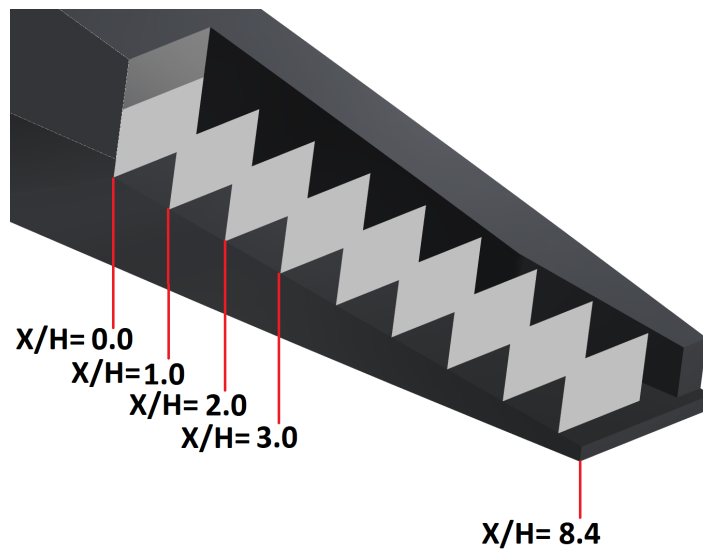


Figure 5.14: X/H Locations

A few sample X/H plane is shown in Figure 5.14 All five cases show similar trends until the location of X/H=7. After this point, the film-cooling effectiveness for the circular case drops more drastically compared to the other cases. At the end of the breakout surface, the film-cooling effectiveness of the airfoil-shaped case stays higher among all cases.

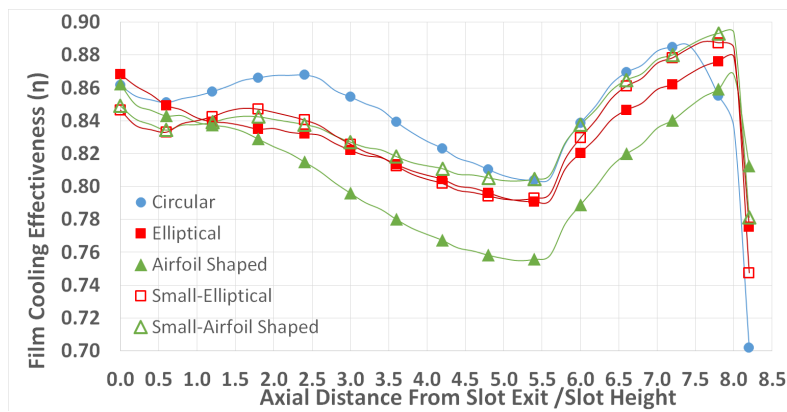


Figure 5.15: Laterally-Averaged Film Cooling Effectiveness on Land Side Wall

Figure 5.15 shows the laterally-averaged film-cooling effectiveness on the side wall of the land. Here, averaging is done over the height of the side wall. As was observed at the breakout surface, on the side of the land elliptical, small elliptical, and small airfoil-shaped pins perform similarly across the region. But in contrast to the breakout surface, the circular pins exhibit the best thermal performance while the airfoil-shaped pins present the lowest average film-cooling effectiveness levels. At $x/H=5.5$, the film-cooling effectiveness for all cases starts increasing. This location is where the breakout surface opens up in the lateral direction. It is likely that this change in the geometry causes the lower-momentum fluid to provide a better coverage on the side walls.

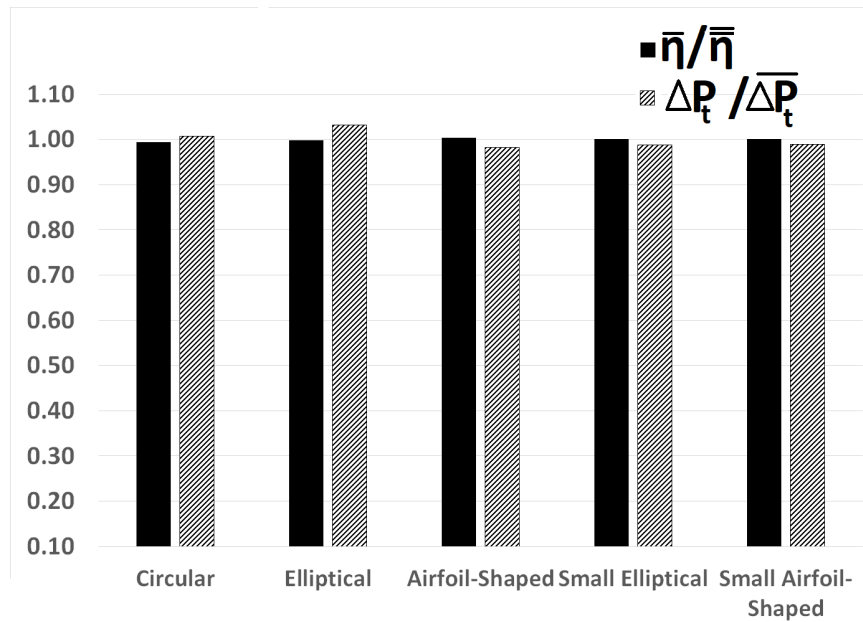


Figure 5.16: Loss And Thermal Comparison Of External Cooling Performance of Pin Arrays

Figure 5.16 summarizes the findings of the external comparison study. The bars filled with diagonal stripes represent the ratio of total pressure loss between the slot exit and the end of the blade (end of the breakout surface) to the average total pressure loss of all five pin arrays. The black bars represent the ratio of the film-cooling effectiveness average for each array to the overall average of all five pin arrays at the breakout region. According to this comparison, the airfoil-shaped and small-sized pins show nearly the same aerothermodynamic performances. For elliptical and circular pin cases, the pressure loss levels are slightly above the average value, while their thermal performances are similar to other three cases. This comparison shows that the overall aerodynamic and thermal performances of film cooling at the breakout surface of the trailing edge region are weakly dependent on the flow structure introduced at the slot exit region.

CHAPTER 6

CONCLUSIONS

This thesis has focused on pin fin and slot film cooling that are commonly used as the means of cooling technology implemented into designs that are working at high-temperature environments. The fluid flow was modeled using the 3D Reynolds-Averaged Navier-Stokes (RANS) equations. The computations were performed to determine the most advantageous combination of shape and size of pin arrays for trailing edge cooling from an aerodynamics and a thermal perspective. For the investigation, the base model with circular pins was taken from the experimental work of Ling et. al [3] and was used for validation purposes. Three different pin shapes of circular, elliptical, and NACA 0033 airfoil profile, and two different pin sizes were considered, resulting in five different models. The flow features, losses, and heat transfer coefficients were compared both inside of the trailing edge section across the pin array and also on the external surface downstream of the slot exit. In defining the pin shapes, the frontal areas and the maximum thicknesses of the shapes were kept the same in order to establish the same amount of blockage area for aerodynamic comparisons. The other option studied was to keep the major axes and the diameter the same. The blockages by the slot exit were of NACA 0033 profile shape, and the airfoil-shaped pins adopted the same profile.

The study is divided into two parts. In the first part, the aerothermodynamic and thermal performances of the pin fins inside the internal cooling channel were investigated. The velocity, pressure, loss variations, heat transfer coefficients and Nusselt number distributions across the flow domain were analyzed for the selected set of boundary conditions. The local features in the flow field showed that the largest total pressure drops occur in and around the pin wakes in the streamwise direction. The

last row of pins, where the elliptical and airfoil-shaped pins stayed relatively closer to the leading edge of the downstream lands and islands, the flow field experienced stronger and wider zones of flow separation resulting in substantial loss generation for this size of pins. The local features showed that the losses keep adding up through the pin array. Despite its larger wetted area, the airfoil-shaped pin was found to have less aerodynamic penalty mostly due to the separation reduction in its wake region, while its thermal performance was at similar levels to those of similar size. On the other hand, the smaller size pins produced less amount of loss as expected; however, this is accompanied with a reduction in thermal performance in return.

In the second part, the investigation has focused on the effects of pin-fin arrays on the flow structure at the slot exit region and the consequences of this structure on the downstream region. The flow conditions generated by different pin arrays at the end of the internal section of the trailing edge were applied at the slot exit as the inlet boundary conditions to the external flow domain of the computations. Minor differences were located in the velocity contours at the breakout region. The stream-wise vorticity contours spanning the downstream region of the trailing edge slot exit revealed that the influence of different coolant inlet conditions starts to diminish approximately around 15 mm downstream of the slot exit, and beyond that point the flow structure for all pin cases behaves similarly. The comparison of pressure coefficients showed that all pin shapes have also very similar pressure loss trends. For the analysis of the thermal performance, heat transfer coefficient, Nusselt number, and film-cooling effectiveness are examined. The small-sized pins demonstrate the highest film-cooling effectiveness at the breakout surface due to lower temperatures at the slot exit. According to the varying aerodynamic and thermal performances of the pins across the internal and external sections, it can be inferred that there is no one correct answer to the selection of the optimal cooling configuration, and the decision should be made according to the needs of the design. On the other hand, performing an optimization on the size of the airfoil-shaped pins would be a promising approach as well.

With the goal of choosing an optimal pin fin configuration that is aerothermodynamically more advantageous for slot film cooling, this thesis provides a through investigation that would be of interest to the turbine designers. The comparison presented

in this paper considers airfoil-shaped pins of NACA 0033 that have not been studied before within an array of pins for similar purposes according to the literature search performed during this thesis work. The circular pins have been commonly used in current designs so far, and there have been studies performed using elliptical pins, although limited in number. The airfoil shape is rather a more novel shape type that has been studied scarcely. With recent advances in the additive manufacturing, however, the implementation of any random shape into the flow path design seems feasible nowadays. For this reason, future studies focusing on either trailing-edge design, or on any component design in general, seem to have room to investigate the use of novel shapes in turbomachinery design.

REFERENCES

- [1] J. Ling and J. Eaton, "Improvements in turbulent scalar mixing modeling for trailing edge slot film cooling geometries: A combined experimental and computational approach.," tech. rep., Sandia National Lab.(SNL-CA), Livermore, CA (United States), 2015.
- [2] J.-C. Han, S. Dutta, and S. Ekkad, *Gas turbine heat transfer and cooling technology*. CRC Press, 2012.
- [3] J. Ling, S. D. Yapa, M. J. Benson, C. J. Elkins, and J. K. Eaton, "Three-dimensional velocity and scalar field measurements of an airfoil trailing edge with slot film cooling: The effect of an internal structure in the slot," *Journal of Turbomachinery*, vol. 135, no. 3, p. 031018, 2013.
- [4] D. Metzger, W. Shepard, and S. Haley, "Row resolved heat transfer variations in pin-fin arrays including effects of non-uniform arrays and flow convergence," in *ASME 1986 International Gas Turbine Conference and Exhibit*, pp. V004T09A015–V004T09A015, American Society of Mechanical Engineers, 1986.
- [5] M. Cakan and M. Taslim, "Experimental and numerical study of mass/heat transfer on an airfoil trailing-edge slots and lands," *Journal of Turbomachinery*, vol. 129, no. 2, pp. 281–293, 2007.
- [6] B. A. Brigham and G. J. VanFossen, "Length to diameter ratio and row number effects in short pin fin heat transfer," *Journal of Engineering for Gas Turbines and Power*, vol. 106, no. 1, pp. 241–244, 1984.
- [7] J. Armstrong and D. Winstanley, "A review of staggered array pin fin heat transfer for turbine cooling applications," *Journal of Turbomachinery*, vol. 110, no. 1, pp. 94–103, 1988.
- [8] S. Arora and W. Abdel-Messeh, "Characteristics of partial length circular

- pin fins as heat transfer augmentors for airfoil internal cooling passages,” in *ASME 1989 International Gas Turbine and Aeroengine Congress and Exposition*, pp. V004T08A008–V004T08A008, American Society of Mechanical Engineers, 1989.
- [9] P. M. Ligrani and G. I. Mahmood, “Variable property nusselt numbers in a channel with pin fins,” *Journal of Thermophysics and Heat Transfer*, vol. 17, no. 1, pp. 103–111, 2003.
- [10] M. Chyu, “Heat transfer and pressure drop for short pin-fin arrays with pin-endwall fillet,” in *ASME 1989 International Gas Turbine and Aeroengine Congress and Exposition*, pp. V004T08A011–V004T08A011, American Society of Mechanical Engineers, 1989.
- [11] D. Metzger, C. Fan, and S. Haley, “Effects of pin shape and array orientation on heat transfer and pressure loss in pin fin arrays,” *Journal of Engineering for Gas Turbines and Power*, vol. 106, no. 1, pp. 252–257, 1984.
- [12] M. Chyu, Y. Hsing, and V. Natarajan, “Convective heat transfer of cubic fin arrays in a narrow channel,” *Journal of Turbomachinery*, vol. 120, no. 2, pp. 362–367, 1998.
- [13] Q. Li, Z. Chen, U. Flechtner, and H.-J. Warnecke, “Heat transfer and pressure drop characteristics in rectangular channels with elliptic pin fins,” *International Journal of Heat and Fluid Flow*, vol. 19, no. 3, pp. 245–250, 1998.
- [14] O. Uzol and C. Camci, “Heat transfer, pressure loss and flow field measurements downstream of staggered two-row circular and elliptical pin fin arrays,” *Journal of Heat Transfer*, vol. 127, no. 5, pp. 458–471, 2005.
- [15] Z. Chen, Q. Li, D. Meier, and H.-J. Warnecke, “Convective heat transfer and pressure loss in rectangular ducts with drop-shaped pin fins,” *Heat and Mass Transfer*, vol. 33, no. 3, pp. 219–224, 1997.
- [16] J. Ling, C. J. Elkins, and J. K. Eaton, “Optimal turbulent schmidt number for rans modeling of trailing edge slot film cooling,” in *ASME Turbo Expo 2014: Turbine Technical Conference and Exposition*, pp. V05BT13A015–V05BT13A015, American Society of Mechanical Engineers, 2014.

- [17] F. Ames and L. Dvorak, “Turbulent transport in pin fin arrays: experimental data and predictions,” *Journal of Turbomachinery*, vol. 128, no. 1, pp. 71–81, 2006.
- [18] P. Martini, A. Schulz, H.-J. Bauer, and C. Whitney, “Detached eddy simulation of film cooling performance on the trailing edge cutback of gas turbine airfoils,” *Journal of Turbomachinery*, vol. 128, no. 2, pp. 292–299, 2006.
- [19] F. Wang, J. Zhang, and S. Wang, “Investigation on flow and heat transfer characteristics in rectangular channel with drop-shaped pin fins,” *Propulsion and Power Research*, vol. 1, no. 1, pp. 64–70, 2012.
- [20] R. Fernandes, M. Ricklick, A. Prasad, and Y. Pai, “Benchmarking reynolds averaged navier–stokes turbulence models in internal pin fin channels,” *Journal of Thermophysics and Heat Transfer*, pp. 1–7, 2017.
- [21] K. K. Ferster, K. L. Kirsch, and K. A. Thole, “Effects of geometry, spacing, and number of pin fins in additively manufactured microchannel pin fin arrays,” *Journal of Turbomachinery*, vol. 140, no. 1, p. 011007, 2018.
- [22] K. L. Kirsch and K. A. Thole, “Pressure loss and heat transfer performance for additively and conventionally manufactured pin fin arrays,” *International Journal of Heat and Mass Transfer*, vol. 108, pp. 2502–2513, 2017.
- [23] F. Cunha and M. K. Chyu, “Trailing-edge cooling for gas turbines,” *Journal of Propulsion and Power*, vol. 22, no. 2, pp. 286–300, 2006.
- [24] S. Kacker and J. Whitelaw, “An experimental investigation of the influence of slot-lip-thickness on the impervious-wall effectiveness of the uniform-density, two-dimensional wall jet,” *International Journal of Heat and Mass Transfer*, vol. 12, no. 9, pp. 1196–1201, 1969.
- [25] S. Sivasegaram and J. Whitelaw, “Film cooling slots: the importance of lip thickness and injection angle,” *Journal of Mechanical Engineering Science*, vol. 11, no. 1, pp. 22–27, 1969.
- [26] T. Horbach, A. Schulz, and H.-J. Bauer, “Trailing edge film cooling of gas turbine airfoils—effects of ejection lip geometry on film cooling effectiveness and heat transfer,” *Heat Transfer Research*, vol. 41, no. 8, 2010.

- [27] T. Horbach, A. Schulz, and H.-J. Bauer, “Trailing edge film cooling of gas turbine airfoils—external cooling performance of various internal pin fin configurations,” *Journal of Turbomachinery*, vol. 133, no. 4, p. 041006, 2011.
- [28] M. Taslim, S. Spring, and B. Mehlman, “Experimental investigation of film cooling effectiveness for slots of various exit geometries,” *Journal of Thermophysics and Heat Transfer*, vol. 6, no. 2, pp. 302–307, 1992.
- [29] N. Fiala, I. Jaswal, and F. Ames, “Letterbox trailing edge heat transfer: Effects of blowing rate, reynolds number, and external turbulence on heat transfer and film cooling effectiveness,” *Journal of Turbomachinery*, vol. 132, no. 1, p. 011017, 2010.
- [30] Z. Yang and H. Hu, “Study of trailing-edge cooling using pressure sensitive paint technique,” *Journal of Propulsion and Power*, vol. 27, no. 3, pp. 700–709, 2011.
- [31] O. Uzol, C. Camci, and B. Glezer, “Aerodynamic loss characteristics of a turbine blade with trailing edge coolant ejection: Part 1—effect of cut-back length, spanwise rib spacing, free-stream reynolds number, and chordwise rib length on discharge coefficients,” *Journal of Turbomachinery*, vol. 123, no. 2, pp. 238–248, 2001.
- [32] O. Uzol and C. Camci, “Aerodynamic loss characteristics of a turbine blade with trailing edge coolant ejection: part 2—external aerodynamics, total pressure losses, and predictions,” *Journal of Turbomachinery*, vol. 123, no. 2, pp. 249–257, 2001.
- [33] D. S. Holloway, J. H. Leylek, and F. A. Buck, “Pressure-side bleed film cooling: Part i—steady framework for experimental and computational results,” in *ASME Turbo Expo 2002: Power for Land, Sea, and Air*, pp. 835–843, American Society of Mechanical Engineers, 2002.
- [34] D. S. Holloway, J. H. Leylek, and F. A. Buck, “Pressure-side bleed film cooling: Part ii—unsteady framework for experimental and computational results,” in *ASME Turbo Expo 2002: Power for Land, Sea, and Air*, pp. 845–853, American Society of Mechanical Engineers, 2002.

- [35] T. Barth and D. Jespersen, "The design and application of upwind schemes on unstructured meshes," in *27th Aerospace Sciences Meeting*, p. 366, 1989.
- [36] F. R. Menter, "Two-equation eddy-viscosity turbulence models for engineering applications," *AIAA Journal*, vol. 32, no. 8, pp. 1598–1605, 1994.
- [37] C. Ansys, "Release 11.0," *ANSYS CFX-Solver Theory Guide*, ANSYS, 2006.
- [38] J. C. Telisinghe, *Film cooling of turbine blade trailing edges*. PhD thesis, University of Oxford, 2013.
- [39] L. Hylton, M. Mihelc, E. Turner, D. Nealy, and R. York, "Analytical and experimental evaluation of the heat transfer distribution over the surfaces of turbine vanes," *NASA Report*, 1983.
- [40] M. J. Benson, C. J. Elkins, S. D. Yapa, J. B. Ling, and J. K. Eaton, "Effects of varying reynolds number, blowing ratio, and internal geometry on trailing edge cutback film cooling," *Experiments in Fluids*, vol. 52, no. 6, pp. 1415–1430, 2012.